

University of Warsaw
Faculty of Physics

Natalia Kuk

Record book number: 382649

Phase coherent laser systems for experiments with cold atoms

Master's thesis
in the field of Physics (Studies in English)

The thesis was written under the supervision of
Dr Mariusz Semczuk
Division of Optics, Institute of Experimental Physics

Warsaw, 09.2021

Summary

Experiments with cold atoms require laser light sources which are highly stable, have good spectral properties and operate at very specific frequencies. In this thesis, we will present the theory and results of experiments in which also phase coherence between laser light sources is required. We achieve phase coherence in semiconductor laser diodes through optical injection locking to the external cavity diode lasers stabilized to atomic transitions. Since injection locking requires relatively low power in comparison to the injection locked laser diodes' output, there is enough power in the system to perform frequency and amplitude modulation with the electro-optical and acousto-optical modulators despite all of the losses. In the thesis, phase coherent lasers operating at 852 nm and serving as sources for cooling and repumping beams are used for performing Λ -enhanced gray molasses cooling and observing electromagnetically induced transparency phenomenon in ultracold cesium atoms. Additionally, an experimental system for performing stimulated Raman adiabatic passage with 852 nm lasers is built and characterized. We also present an all-fiber laser module injection locked to a master fiber laser operating at 1064 nm through an optical circulator. This module's output power enables seeding of multiple high-power amplifiers.

Key words

phase coherence, optical injection locking, Λ -enhanced grey molasses cooling, EIT, STIRAP

Title of the thesis in Polish language

Lasery spójne fazowo do eksperymentów z zimnymi atomami.

Contents

Thesis overview	3
1. Introduction	4
1.1. Coherence of light	4
1.2. Phase coherent beams via optical injection locking	5
1.3. Laser cooling and trapping	8
1.3.1. Magneto-optical trap	8
1.3.2. Gray molasses cooling	10
1.4. Coherent manipulation	13
1.4.1. Λ -enhanced gray molasses cooling	13
1.4.2. Stimulated Raman Adiabatic Passage	14
1.4.3. Electromagnetically induced transparency	16
2. Cesium laser systems	18
2.1. Laser system preparation for Λ -enhanced gray molasses	18
2.1.1. Electro-optical modulator	18
2.1.2. Laser system operation	20
2.2. STIRAP and EIT experimental setup	22
2.2.1. Laser system	22
2.2.2. Acousto-optical modulator	24
2.2.3. Generation of optical pulses	25
2.3. Injection locking of cesium lasers	29
3. All-fiber 1064 nm laser module	32
3.1. Fiber components	32
3.2. Design and assembly	33
3.3. Performance	36
4. Observation of coherent phenomena	38
4.1. Λ -enhanced gray molasses cooling	38
4.2. Observation of electromagnetically induced transparency	40
5. Summary	44

Thesis overview

This thesis focuses on implementation of optical injection locking technique for generation of frequency detuned phase coherent laser light beams. We present laser setups with slave semiconductor lasers designed and built in the Quantum Gases Laboratory, which are injection locked with light from commercial master lasers.

The first chapter is a review of methods and tools used in the thesis. It introduces the idea of phase coherence and methods for obtaining it with the focus on optical injection locking technique, since it is implemented in all of the experimental setups presented in following chapters. We briefly discuss laser cooling and trapping and give a description of exemplary cold atom experiments which require phase coherent light fields such as Λ -enhanced gray molasses cooling, stimulated Raman adiabatic passage and electromagnetically induced transparency.

The second chapter presents experimental setups composed of lasers operating at 852 nm. They are designed to generate frequencies addressing atomic transitions needed for the implementation of state manipulation techniques exploiting phase coherence. Two semiconductor lasers (called slaves) have been built such that each one can be injection locked by the light from a frequency stabilized external cavity diode laser (called master). The characterization of performance of the slave lasers is reported when they are both directly injection locked to the master laser light and when one of them is locked to a sideband of a master laser light modulated by an electro-optical modulator.

The third chapter gives details of the design, assembly and performance of an all-fiber 1064 nm slave laser module injection locked with light from a highly stable fiber laser. The module is used for seeding a high-power fiber amplifier whose output is used in dipole trapping of atoms. The module's output power is about ten times higher than that of the master laser, thus in the future work it might enable seeding more than one amplifier, eliminating the need to purchase another seed laser. This enables an additional application: phase coherent addition of light from several high power fiber amplifiers.

In the fourth chapter, the results of two experiments with cold cesium atoms requiring phase coherence are presented. The first experiment is Λ -enhanced gray molasses cooling, a sub-Doppler cooling technique which has been implemented for the first time in our laboratory. The other presented experiment is observation of electromagnetically-induced transparency in an ultracold atomic gas - a test bed for the experimental setup constructed to perform stimulated Raman adiabatic passage between cesium ground state hyperfine levels.

Chapter 1

Introduction

In this Chapter, we will introduce the reader to the idea of coherence of light and to the methods to obtain phase coherence between two laser beams which differ in frequency. One of the methods that is used extensively in the experiments reported in this thesis, optical injection locking, will be described in more details. Next, a brief introduction to laser cooling and magneto-optical trapping will be given with an emphasis on reaching sub-Doppler temperatures. Finally, we will discuss three exemplary atom manipulation techniques that rely on phase coherence of laser fields: Λ -enhanced gray molasses cooling (Λ_{GMC}), electromagnetically induced transparency (EIT) and stimulated Raman adiabatic passage (STIRAP). Experimental setups built to implement these techniques are described in Chapter 2 and the experimental realization of the first two is demonstrated in Chapter 4.

1.1. Coherence of light

Experiments in the field of atomic and molecular physics rely on laser light sources of well defined frequency to address atomic or molecular transitions of interest. These sources should have small power fluctuations and provide stable frequency output with low jitter and a linewidth at least comparable with the linewidth of the transitions that they are supposed to excite. Long term instabilities introduce fluctuations of the experimental results like a shot-to-shot variation, a drift in the captured atom number, or a decrease in the transfer efficiency between quantum states when the frequency of the laser field drifts away from probed transition. Short term instabilities can also be detrimental. For example, a sudden light frequency change might cause excitation to an atomic or molecular state which was not accounted for in the experiment.

The quality of light can be measured in terms of its temporal and spatial coherence [1]. A measure characterizing the temporal coherence is the coherence time τ_c which is related to the coherence length by the relation $L_c = c\tau_c$, where c is the speed of light. It can also be quantified using the first order correlation function:

$$g^{(1)}(\tau) = \frac{\langle \mathcal{E}^*(t)\mathcal{E}(t+\tau) \rangle}{\langle |\mathcal{E}(t)|^2 \rangle} \quad (1.1)$$

where the numerator:

$$\langle \mathcal{E}^*(t)\mathcal{E}(t+\tau) \rangle = \frac{1}{T} \int_T \mathcal{E}^*(t)\mathcal{E}(t+\tau) dt \quad (1.2)$$

is an average taken over a long time interval T . At $\tau=0$, the correlation function is equal to one and it is close to one for times much lower than τ_c . However, as τ increases the phase

becomes more random and the correlation function decreases, eventually dropping to zero for times much longer than τ_c . The coherence time can be expressed in terms of the correlation function as [2]:

$$\tau_c \equiv \int_{-\infty}^{\infty} |g^{(1)}(\tau)|^2 d\tau \quad (1.3)$$

but it can also be approximated as $\tau_c = 1/(\pi\Delta\nu)$, where $\Delta\nu$ is the linewidth of the light source. A prime example of sources of coherent light are lasers, which can be designed to emit extremely stable frequencies with some of the external cavity diode lasers reaching a free-running linewidth of several kHz [3], which corresponds to the coherence time approaching 1 ms and coherence length of ~ 300 km. The coherence length can be improved even further if a laser is actively stabilized to a reference like a narrow atomic or molecular transition, or a silicon Fabry-Perot cavity. In fact, a Matei et al. [4] reported a system emitting at 1542 nm with a coherence length exceeding several million kilometers and coherence time estimated to fall between 11 s and 55 s.

The equation 1.3 can also be used to deduce the degree of coherence for a superposition of fields with different frequencies, e.g. two independent lasers. We can write down the electric field component for the first source as:

$$\mathcal{E}_1(t) = \mathcal{E}_1 \exp(i\omega t) \quad (1.4)$$

and:

$$\mathcal{E}_2(t) = \mathcal{E}_2 \exp(i((\omega + \Delta)t + \phi)) \quad (1.5)$$

for the second one, where \mathcal{E}_1 and \mathcal{E}_2 are electric field amplitudes and ω is the angular frequency. The sources are characterized by a frequency difference Δ and a phase difference ϕ . The resulting degree of coherence for two separate modes can be expressed as [5]:

$$|g^{(1)}(\tau)| = \sqrt{\mathcal{E}_1^2 + \mathcal{E}_2^2 + 2\mathcal{E}_1\mathcal{E}_2 \cos(\Delta \cdot \tau + \phi)} \quad (1.6)$$

For two independent light sources, ω , Δ and ϕ will vary in time due to environmental factors such as temperature, pressure or humidity changes, mechanical vibrations of the laser cavity or instabilities of the power supply. However, when Δ and ϕ are made constant then the sources will become phase coherent. The function presented in equation 1.6 is periodic with frequency Δ and it reaches some maximum value every period. This maximum acts as the correlation measure, it decreases as τ increases, eventually dropping to zero, meaning that the light is no longer coherent.

1.2. Phase coherent beams via optical injection locking

Injection locking method will be widely used in this thesis as a method to guarantee phase coherence between different light sources. Before we focus on its description, first we will give a brief overview of some of the methods that can, in principle, give a similar result in terms of the phase coherence between laser fields:

1. **Splitting the beam of a single laser into two (or more) paths.** This is the most straightforward approach which guarantees, under proper conditions, the phase coherence between individual paths. The optical path lengths should not differ by more than a fraction of the coherence length of the laser. In practical situations another limitation needs to be kept in mind as well: each path could in principle experience

different environmental conditions (e.g. vibrations of optical elements or parameters of optical fibers used to propagate the beams) which could have a detrimental effect on the phase, especially in the long term.

2. **Splitting the beam of a single laser into two (or more) paths and adding frequency shifting elements to chosen paths.** This is a fairly convenient way to generate laser fields with frequency difference on the order of several hundred MHz. Acousto-optic devices (AOD) are commonly used for this purpose (more on that in Subsection 2.2.2). The drawback is that the frequency shifting comes at a price of decreasing the available power: a single pass through an AOD decreases the available power by 5% to 50%, depending on the specific device used. For large frequency shifts requiring multiple passes, the power loss can become an issue very quickly but in many applications this is not necessarily a problem if the overall simplicity of the setup is the most important [6, 7, 8, 9, 10]. If frequency shifting is done in more than one path, one needs to make sure that rf sources driving each acousto-optic device are also phase coherent, otherwise rf signals' relative phase fluctuation would cause corresponding phase fluctuations of the optical fields.
3. **Using an electro-optical modulator (EOM) which modulates the phase of the light injected into it.** The radio-frequency or microwave signal applied to drive an EOM leads to the creation of sidebands in the light frequency spectrum. The detuning from the central frequency and the amplitude of a sideband depend on the driving signal's frequency and power (see Subsection 2.1.1). EOMs do not allow for the spatial separation of different frequency components but comparing to AODs they can provide a much higher absolute frequency differences between the light at the input and its components at the output, especially if higher order sidebands can be efficiently generated. In practice, it is often possible to assure that unwanted sidebands (or the carrier) are far detuned from the transition(s) of interest so lack of spatial separation of frequency components is not necessarily an issue.
4. **Optical phase-locked loop (OPLL).** It stabilizes the relative phase and frequency between two lasers by synchronizing them to a reference signal [11]. The error signal in an optical phase-locked loop is derived from a beat-note signal between the two lasers. Practical limitations are imposed by the availability of high speed photodetectors for beat note detection and frequency mixers and other electronics needed to process microwave signals. As a result it is rarely used for frequency differences above 10-20 GHz. There is no power loss involved beyond what is needed to obtain a beat note signal but both lasers need to have cavities with frequency tuning components.
5. **Stabilizing lasers to different teeth of an optical frequency comb.** Here, each laser is phased locked to a different tooth of an optical frequency comb [12]. Such combs are based on femtosecond oscillators [13] and their spectrum can easily reach tens of nm. Moreover, high peak intensity of each pulse enables efficient frequency conversion which results in the presence of frequency components that can differ by hundreds of THz. If the beatnote between each continuous-wave laser and a comb tooth is stabilized with an optical phase-locked loop, it guarantees phase coherence between the lasers because there is a well defined phase relation between individual teeth present in the comb's frequency spectrum. The frequency separation of the phase locked lasers is only limited by the available spectrum of the comb and the quality of its stabilization.

6. **Stabilizing lasers to an optical resonator.** If two separate lasers are stabilized to the same Fabry-Perot cavity using, for example, a Pound-Drever-Hall technique [14] it is possible to make them phase coherent. The cavity, however, needs to be properly engineered to provide a large finesse (typically 10^4 or more) at both wavelengths [15]. Overall, this is a rather straightforward and reliable method that is frequently used to obtain phase coherence between lasers used for the production of ultracold ground state molecules [15].
7. **Optical injection locking (OIL).** It requires a master laser, which is the source of the seeding light and a slave laser with a cavity to which the seeding light is injected. Under proper conditions, the slave laser synchronizes with the master, reproducing its spectral properties. Optimizing these conditions such as frequency difference between sources, efficiency of coupling of the seeding light into the slave's cavity and slave's operating current and temperature is crucial for successful injection locking. Here, the slave laser does not require frequency tuning elements in its cavity, which is an important simplification over the OPLL method.

The optical injection locking is based on injecting the master laser's seeding light with desired properties to the cavity of a slave laser. Sending the seeding light to the cavity is usually realised through a special port of an optical isolator or, in some cases, through an optical circulator (it's operation will be described in section 3.1) - this minimizes back-reflections of the slave output to its laser diode's cavity which can have detrimental effects on its operation. Uncontrolled back reflections can introduce unwanted modes' enhancement or they can even cause laser diode's failure [16]. There are number of factors that influence injection locking success; the model is described in [17]. It introduces additional terms to the laser rate equations to take into consideration the impact of seeding light:

$$\frac{dA(t)}{dt} = \frac{1}{2}g [N(t) - N_{\text{th}}] A(t) + \kappa A_{\text{inj}} \cos(\phi(t)) \quad (1.7)$$

$$\frac{d\phi(t)}{dt} = \frac{\alpha}{2}g [N(t) - N_{\text{th}}] - \kappa \frac{A_{\text{inj}}}{A(t)} \sin \phi(t) - \Delta\omega \quad (1.8)$$

$$\frac{dN(t)}{dt} = J - \gamma_N N(t) - (\gamma_p + g[N(t) - N_{\text{th}}])A(t)^2 \quad (1.9)$$

where $A(t)$ is the field amplitude of the slave laser, A_{inj} is the field amplitude of the injected light, $\phi(t)$ is the phase difference between master's and slave's light, $\Delta\omega$ is the angular frequency difference between the master and the free-running slave, $N(t)$ is the number of carriers in the slave laser (electrons and holes in case of a semiconductor laser), N_{th} is the threshold carriers number, g is the laser gain coefficient, κ is a coefficient that describes coupling of the seeding light to the laser diode's cavity and α is the linewidth enhancement factor which quantifies coupling between the variations of optical frequency and variations in carrier population [18]. In the equation 1.9, J is the pump current, γ_N is the carrier recombination rate and γ_p is the decay of the photons in the cavity.

From these equations, a region for which stable injection locking occurs can be derived by considering the steady state solution of rate equations (1.7-1.9). Injection locking can be observed within the locking range, $\Delta\omega_{LR}$:

$$-\kappa \sqrt{1 + \alpha^2} \sqrt{\frac{P_{\text{inj}}}{P_o}} = \omega_{\text{min}} < \Delta\omega_{LR} < \omega_{\text{max}} = \kappa \sqrt{\frac{P_{\text{inj}}}{P_o}} \quad (1.10)$$

Thus, the injection locking depends on the linewidth enhancement factor α and on κ , which widens the injection locking range when more seeding light photons circulate inside the slave's optical cavity. It depends also on the P_{inj}/P_o ratio where P_{inj} is the injected light power and P_o is the slave's output power.

An important advantage of injection locking is that the linewidth of the slave laser can be significantly reduced with respect to its free running value, reaching the same level as the linewidth of the master laser. It is also relatively low-cost and low-noise method of light amplification since very little seeding power (as little as nW fraction in some applications [19]) is needed compared to the slave's output. It makes this method very attractive for the purposes where stability, spectral quality and phase coherence of light is of high importance. From the technical standpoint, the slave laser can be based on a laser diode without any additional frequency selective components or frequency stabilizing electronics, therefore it is much easier and cheaper to construct than designs with an external cavity.

The OIL method is widely employed in the field of atomic and molecular physics. It is used for generating spectrally pure light by injection locking high power laser diodes [20] which can result in amplification of the order of 44 dB. Injection locking with an EOM's sideband has been also reported for generating Raman beams for atom interferometry [21, 22] and laser frequency sweeping by scanning the RF signal applied to the EOM [23].

1.3. Laser cooling and trapping

In this section, we introduce the basics of laser cooling and trapping such as magneto-optical trap and Doppler laser cooling limit. It is followed by the description of optical molasses, one of sub-Doppler cooling techniques, which will be later important to understand the principle of Λ -enhanced gray molasses cooling and how phase coherence of light sources influences its performance.

1.3.1. Magneto-optical trap

The magneto-optical trap (MOT) is a basic tool in cold atoms experiments. It uses optical and magnetic potentials to trap an atomic cloud. The light itself can slow the atoms but the combination of the light and magnetic potential can both cool them and spatially-localize in the trap. In a standard magneto-optical trap there are three, mutually orthogonal pairs of counter-propagating beams that cross at the center, forming three-dimensional potential, as pictured in Fig. 1.1a. Since the Doppler cooling is isotropic and occurs at the same rate regardless of position, the trapping is not yet achieved. Magnetic field introduces a potential minimum in which the atomic cloud is formed, thus enabling trapping. Two coils in the anti-Helmholtz configuration create a quadrupole potential, which magnitude decreases towards the center of the trap. The crossing of the cooling beams is overlapped with the center of the magnetic field. The beams are red-detuned with respect to a cooling transition and their polarizations are circular, chosen in such a way that they only excite transitions which will effectively push atoms into towards the center of the magnetic field. However, the Zeeman splitting and Doppler cooling effects have to be well balanced to perform magneto-optical trapping. If the temperature and density of atoms at the trap's center is too high, collisions between them will cause losses. These parameters must be well-optimized in order to steadily trap atoms in the potential minimum. As shown in Fig. 1.1b for a simplified atom, the magnetic field amplitude and direction has impact on the splitting of Zeeman levels according to the formula [24]:

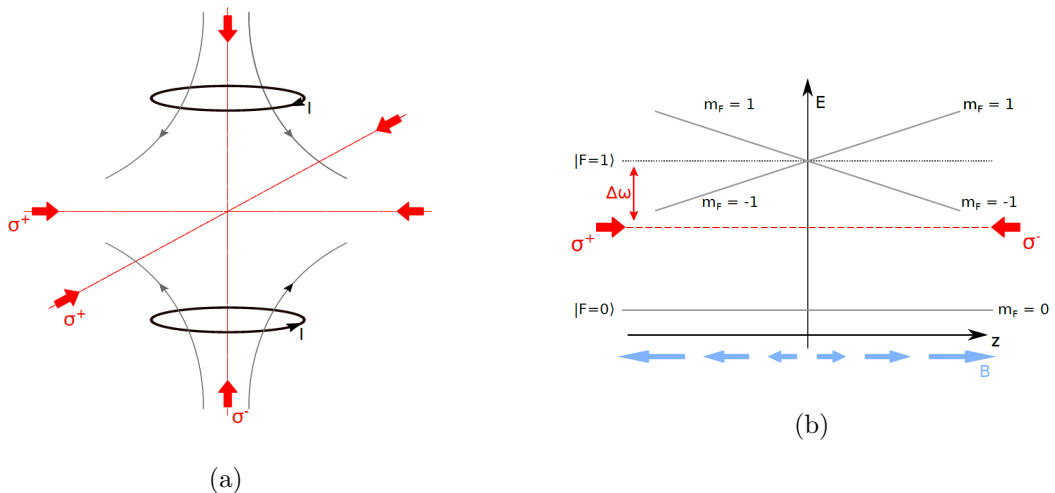


Figure 1.1: a) An scheme of a 3-dimensional magneto-optical trap. Two coils in the anti-Helmholtz configuration create a quadrupole magnetic field with minimum at the trap's center. Three perpendicular pairs of counter-propagating, circularly polarized beams cross each other in the trap center. Note that the polarization of one of the pairs is orthogonal to the rest due to the magnetic field pointing inwards. b) Zeeman splitting of an exemplary excited state $F = 1$, dependent on the spatial change of the magnetic field along the optical axis z . $\Delta\omega$ is the angular frequency difference of the $m_F = -1$ level from the case when no magnetic field is applied. Pictures taken from [25].

$$\Delta E_{m_F} = \mu_B g_F m_F B_z \quad (1.11)$$

where μ_B is Bohr magneton, g_F is the Landé g -factor, m_F ($-F \leq m_F \leq F$) is a projection of the total angular momentum F on the quantization axis set by the direction of the magnetic field B (here assumed to be the z -axis). The selection rules for transitions between Zeeman levels state that σ_- polarized light excites atom in m_F state to $m_F - 1$ state, π light does not induce change of m_F in the excited state, and an excitation with σ_+ changes m_F to $m_F + 1$.

For example, cesium atoms which will be under investigation in this thesis, have a hyperfine structure due to the $I = 7/2$ spin of its nucleus. It results in the presence of two hyperfine levels in the $S_{1/2}$ ground state and four hyperfine levels in the excited $P_{3/2}$ state, which can be seen in Fig. 1.2. Atomic transitions induced by light are described by the electric-dipole approximation. Its selection rules impose that $F \rightarrow F' = F, F \pm 1$ transitions are allowed. Assuming that the cooling (pumping) light is chosen to be near-resonant with the $F = 4 \rightarrow F' = 5$ transition, most of the atoms interacting with light will be excited to the $F' = 5$ excited state. Nevertheless, the $F = 4 \rightarrow F' = 5$ transition is not a fully closed one, because there is a non-negligible probability of off-resonance excitations to the $F' = 4$ state which causes leakage of population into the $F = 3$ ground state. It introduces necessity for a repumping light beam, near-resonant with the $F = 3 \rightarrow F' = 4$ transition that would enable atoms in $F = 3$ ground state to come back to the cooling cycle.

The temperatures obtained in the magneto-optical traps are dependent on the species that are trapped e.g. around $100 \mu\text{K}$ for cesium [27], $150 \mu\text{K}$ for rubidium [28], $140 \mu\text{K}$ for potassium-39 and potassium-41 [29], $63 \mu\text{K}$ for fermionic potassium-40 [30], 0.25 mK for metastable helium [31] and $6 \mu\text{K}$ for metastable strontium [32]. These are typically below the temperature called a Doppler limit, T_D [33]:

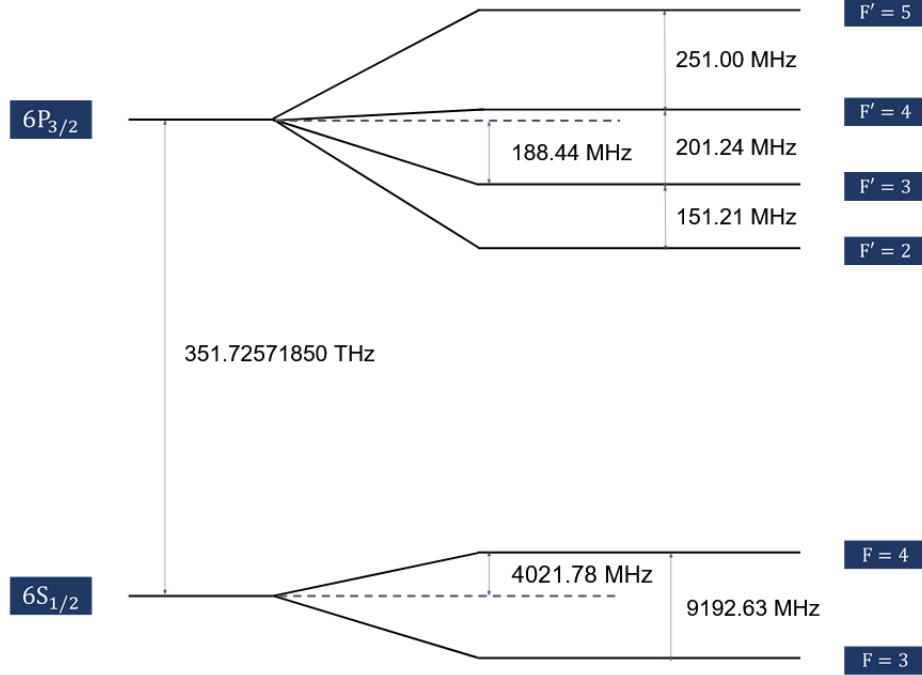


Figure 1.2: Hyperfine structure of cesium, D2 line. The data for the diagram were taken from [26].

$$k_B T_D = \frac{\hbar \Gamma}{2} \quad (1.12)$$

where k_B is the Boltzmann constant and Γ is the natural linewidth of the cooling transition. To reach lower temperatures, more advanced sub-Doppler cooling techniques have to be implemented [33].

1.3.2. Gray molasses cooling

Temperatures lower than the ones that could be obtained in a magneto-optical trap are necessary for efficient transport of atoms to conservative traps and performing experiments such as photoassociation and magnetoassociation of molecules, or cooling atoms down to quantum degeneracy. There are several methods to reduce the temperature of atoms, one of them being optical molasses, a sub-Doppler technique which enables cooling down to temperatures even three orders of magnitude lower than obtained in a magneto-optical trap. This method uses counter-propagating beams detuned from an atomic transition to exert a viscous damping force on moving atoms. Since the beams propagate back and forwards, the atoms experience deceleration regardless of their movement direction along the axis of molasses' beams. Depending on the number of beams introduced in optical molasses, it can be either one-, two- or three-dimensional (six beams propagating on three axes).

In the late 1980s, group lead by P. D. Lett studied the behaviour of atoms in optical molasses [34]. Result of one of their experiments surpassed their expectations when they managed to cool Na atoms down to 40 μ K, below the Doppler limit of 240 μ K. It was also observed that the temperature was sensitive to the beam polarization, magnetic field changes and detuning dependence, deviating from the Doppler theory. As no theory for cooling below

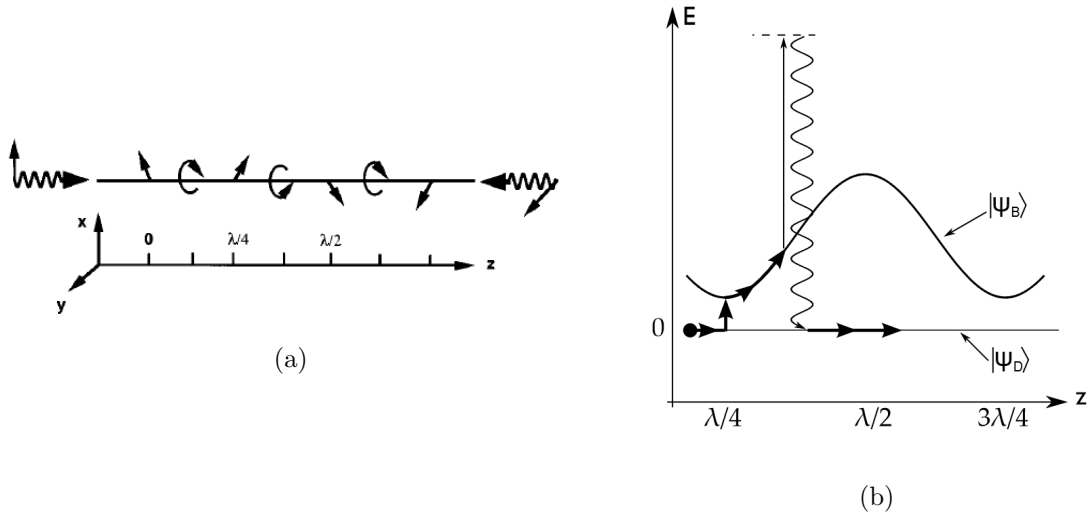


Figure 1.3: a) Periodic change of polarization along the optical axis when two counter-propagating beams with orthogonal linear polarizations are overlapped. Figure taken from [33]. b) Scheme of the polarization gradient cooling procedure. An atom moves from the dark to the bright state when the potential barrier is the lowest. It climbs the potential hill loosing its kinetic energy. It is excited from the hillside, relaxes to the dark state and repeats the whole cycle. Figure taken from [35].

Doppler limit had been created before, the finding has began a wide investigation within the scientific community involved in laser cooling. It led to formulating a theory of gray molasses cooling, a phenomenon that combines polarization gradient cooling and optical pumping to uncoupled from light-matter interactions "dark" states, as these interactions are main source of heating in conventional methods. The idea is presented schematically in Figure 1.3b. Two counter-propagating beams with orthogonal polarizations create polarization gradient that changes with position along beams' axis like in Figure 1.3a. It periodically alters from σ_+ to lin, and to σ_- being elliptical in between. As a result, coupling of different magnetic sub-levels is characterized by varying coupling strength which is dependent on the local polarization, hence also on the position.

In the part below, we will consider gray-molasses cooling in the three-level Λ -system. The Λ -system, shown in Figure 1.4, is a system in which transition between two lowest levels is electric-dipole forbidden, while the transitions from these two lower states to the highest one is the electric-dipole allowed transition.

In such a system where the lowest $|1\rangle$ state's energy is considered to be 0, Hamiltonian of a free-atom can be written as:

$$\hat{H}_A = \hat{H}_{kin} + \hat{H}_0 = \frac{\hat{p}^2}{2m} + \hbar E_2 |2\rangle\langle 2| + E_3 |3\rangle\langle 3| \quad (1.13)$$

where m is atom's mass, \hat{p} is atomic momentum operator and E_3 is the energy of that atom possesses in the excited state $|3\rangle$ and E_2 is the energy of atom in state $|2\rangle$. The atom-light interaction in rotating wave approximation is described by:

$$\hat{V} = \left(\frac{\hbar\Omega_{13}}{2} |3\rangle\langle 1| + \frac{\hbar\Omega_{23}}{2} |3\rangle\langle 2| \right) \exp(-i\omega t) + h.c. \quad (1.14)$$

Where $\omega \approx \omega_{13} \approx \omega_{23}$, ω_{ij} being frequency of light resonant with $|i\rangle$ to $|j\rangle$ transition, Ω_{13}

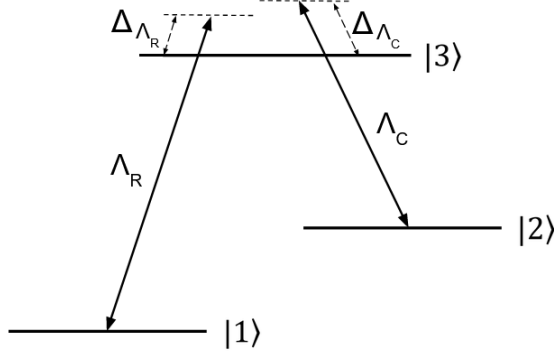


Figure 1.4: Three-level Λ -system with $|1\rangle \rightarrow |3\rangle$ and $|2\rangle \rightarrow |3\rangle$ dipole-allowed transition and $|1\rangle \rightarrow |2\rangle$ forbidden transition. Δ_{Λ_R} is the one-photon detuning of Λ_R repumping light frequency and Δ_{Λ_C} is the one-photon detuning of Λ_C cooling light frequency.

and Ω_{23} are the Rabi frequencies - coupling constants between atom and laser light in the form:

$$\Omega_{13/23} = -\frac{\hat{d}_{13/23}\hat{\mathcal{E}}_{13/23}}{\hbar} \quad (1.15)$$

$d_{13,23}$ dipole moment of $|1\rangle \rightarrow |3\rangle$ / $|2\rangle \rightarrow |3\rangle$ transition and $\hat{\mathcal{E}}_{13/23}$ being the $|1\rangle \rightarrow |3\rangle$ / $|2\rangle \rightarrow |3\rangle$ transition resonant laser electric field amplitude. When the two photon detuning condition $\Delta_{\Lambda_R} = \Delta_{\Lambda_C}$ is met between the two beams illuminating the atoms, a new basis for the eigen states in this Λ -system can be specified. It is a superposition of bare atomic ground states:

$$|\Phi_D\rangle = \frac{\Omega_{23}}{\Omega}|1\rangle - \frac{\Omega_{13}}{\Omega}|2\rangle, \quad |\Phi_B\rangle = \frac{\Omega_{13}}{\Omega}|1\rangle + \frac{\Omega_{23}}{\Omega}|2\rangle \quad (1.16)$$

where $\Omega = \sqrt{\Omega_{13}^2 + \Omega_{23}^2}$, $|\Phi_D\rangle$ is so called dark state, which does not couple to the excited state $|3\rangle$, $\langle 3|\hat{V}|\Phi_D\rangle = 0$, and $|\Phi_B\rangle$ is the bright state from which excitation to state $|3\rangle$ can happen, $\langle 3|\hat{V}|\Phi_B\rangle = \hbar\Omega/2$.

Nevertheless, \hat{V} is only a part of the total Hamiltonian. Its other part is the kinetic term including momentum. This kinetic part couples dark and bright states as follows:

$$\langle \Phi_B(p)|\frac{\hat{p}^2}{2m}|\Phi_D(p)\rangle = -2\hbar\frac{\Omega_{13}\Omega_{23}}{\Omega^2}\frac{kp}{m} \quad (1.17)$$

where $p = mv$ is proportional to the speed of an atom and k is a wavevector of the light field resonant with $|2\rangle \rightarrow |3\rangle$ transition. Dark state's lifetime τ_D is dependent on the atomic velocity and is proportional to $1/(vk)^2$, thus it can be noticed that the slow atoms will stay in this state longer, while fast atoms will transit to the bright state faster. The kinetic energy of atoms effectively decreases since the slow, cold atoms stay slow, while the fast atoms still undergo the cyclic process of cooling.

The probability of transition from dark to the bright state is equal to the square of expression 1.17. From the formula it can be seen that another factor influencing the probability that an atom moves from dark to the bright state is change in light frequency since wavevector k will be influenced. Wavevector k can be expressed as: $k = (\omega_{23} + \Delta_{\Lambda_C})/c$, thus the transition probability increases proportionally with the square of Δ_{Λ_C} .

1.4. Coherent manipulation

In this section we will mention about Λ -enhanced grey molasses cooling, stimulated Raman adiabatic passage and electromagnetically induced transparency experiments for which the experimental setups are built and described later in the thesis. These processes are based on quantum interference of bare atomic states under the influence of electromagnetic radiation, which leads to creating a dark state. The nature of these phenomena introduces need for phase coherent light sources. In STIRAP, existence of this dark state is used for efficient and selective population transfer between two quantum states while in the EIT we will focus mainly on its abilities to block the population transfer between two specified states.

1.4.1. Λ -enhanced gray molasses cooling

In Λ -enhanced gray-molasses cooling in a three-level Λ -system, the same mechanisms occur as in grey molasses cooling described in section 1.4.1. However, this time the light beams are both blue-detuned and meet zero two-photon condition, $\Delta_{\Lambda_C} = \Delta_{\Lambda_R}$ in scheme from Figure 4.1. It was reported that in such a system, the cooling process was enhanced [36].

Performing Λ -enhanced gray molasses cooling was reported for species like fermionic ^{40}K [37], ^{39}K [38], ^{41}K [39], Cs D2 line [40], ^7Li D1 line [41] and ^{87}Rb [36]. In a publication from 2017 [36], Λ -enhanced grey molasses were shown on the D2 line of ^{87}Rb a thorough analysis of the phase coherence of lasers was performed. Some of the results are shown in Figure 1.5. It shows that lower temperatures were obtained while the light sources used in the experiment were phase coherent. This feature also led to higher phase-space density.

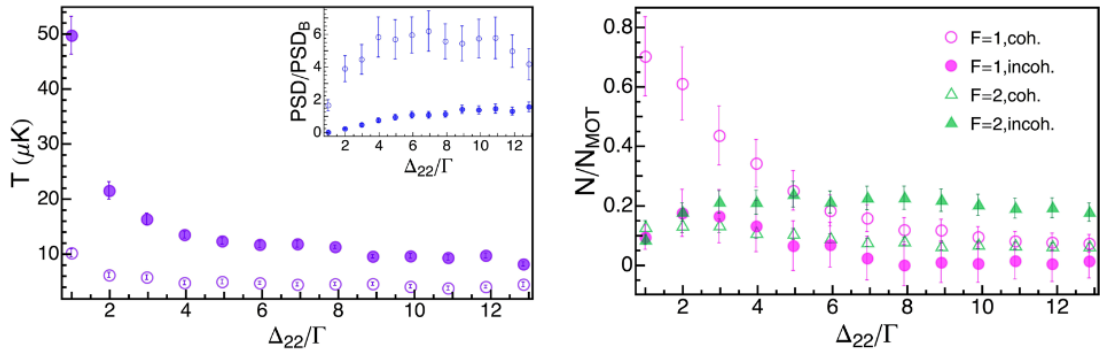


Figure 1.5: Presentation of influence of lasers' phase coherence and detuning in Λ -enhanced grey molasses cooling experiment performed on cold rubidium atoms [36]. On the left: temperature dependence on the detuning between cooler and repumper, empty points - coherent laser, filled points - incoherent lasers. $F = 1, F = 2$ are the hyperfine levels of $5^2S_{1/2}$ state of rubidium, while $F' = 2$ is one of the $5^2P_{3/2}$ state's levels. Cooler and repumper are blue-detuned correspondingly from the $F = 2 \rightarrow F' = 2$ and $F = 1 \rightarrow F' = 2$ transition. On the right: Number of atoms in $F=1$ state (pink circles) and $F=2$ state (green triangles) relative to number of atoms in MOT as a function of the detuning between cooler and repumper. Empty markers correspond to measurements performed while lasers were coherent while filled markers indicate that during the measurement lasers were incoherent. Figure is taken from the source publication.

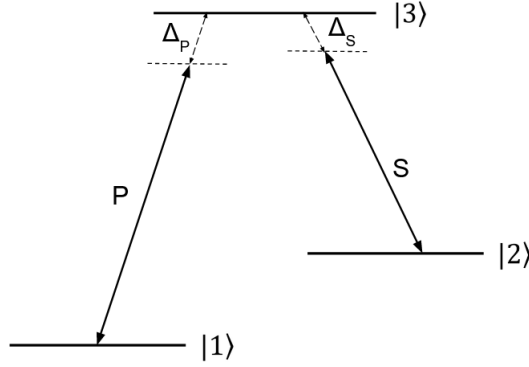


Figure 1.6: Three-level Λ -system with $|1\rangle \rightarrow |3\rangle$ and $|2\rangle \rightarrow |3\rangle$ dipole-allowed transition and $|1\rangle \rightarrow |2\rangle$ forbidden transition. The STIRAP pulse performed on $|1\rangle \rightarrow |3\rangle$ transition is referred as P and the pulse performed on $|2\rangle \rightarrow |3\rangle$ transition is referred as S. Δ_P is the one-photon detuning of P light frequency and Δ_S is the one-photon detuning of S light frequency.

1.4.2. Stimulated Raman Adiabatic Passage

Stimulated Raman Adiabatic Passage is a very useful tool in the field of atomic and molecular physics. It allows for efficient population transfer between two states with use of intermediate third state which does not get populated during the process thus the losses connected to fluorescence are minimized. The transition is induced by pulses of coherent light fields and the dynamics of atoms can be described by time-dependent Schrödinger equation:

$$i\hbar \frac{d}{dt} \Phi(t) = \hat{H}(t) \Phi(t) \quad (1.18)$$

where $\hat{H}(t)$ is the Hamiltonian describing the system and interactions with light pulses, which under rotating-wave approximation can be written as presented below with $\Omega_P(t)$ and $\Omega_S(t)$ being Rabi frequencies dependent on the dipole interaction with light, the energy of which is $-dE(t)$. The d stands for dipole moment operator and $E(t)$ is the electric field of the light. The energy levels scheme is shown in Figure 1.6. The Hamiltonian can be written in the matrix form as:

$$\hat{H}(t) = \frac{1}{2}\hbar \begin{bmatrix} 0 & 0 & \Omega_P(t) \\ 0 & 2\Delta & \Omega_S(t) \\ \Omega_P(t) & \Omega_S(t) & 2\Delta_P \end{bmatrix} \quad (1.19)$$

The two Rabi frequencies can be written as:

$$\Omega_P(t) = -\hat{d}_{13}\hat{\mathcal{E}}_P(t)/\hbar, \quad \Omega_S(t) = -\hat{d}_{32}\hat{\mathcal{E}}_S(t)/\hbar \quad (1.20)$$

where d_{13} and d_{32} are dipole transition operators for $|1\rangle \rightarrow |3\rangle$ and $|2\rangle \rightarrow |3\rangle$ transitions and $\mathcal{E}_P(t)$ and $\mathcal{E}_S(t)$ describe slowly-varying amplitudes of P and S pulses' electric fields. Spontaneous emission from state $|3\rangle$ to states $|1\rangle$ and $|2\rangle$ is possible and undesirable due to its decoherence effects and population transfer efficiency decrease. The lasers' detunings Δ_P and Δ_S from the states that they are close to resonance with can be described as:

$$\hbar\Delta_P = E_3 - E_1 - \hbar\omega_P, \quad \hbar\Delta_S = E_3 - E_2 - \hbar\omega_S \quad (1.21)$$

where $E_3 - E_1$ and $E_3 - E_2$ give values of the energy differences between the corresponding states and ω_P, ω_S are light frequencies. One of the STIRAP requirements is that the two-photon detuning Δ is equal to 0, which means that in the Λ -system the two single-photon detunings are equal, $\Delta_P = \Delta_S$. When this requirement is met, Hamiltonian eigenstates are [42]:

$$|a^0\rangle = \cos \vartheta |1\rangle - \sin \vartheta |2\rangle \quad (1.22)$$

$$|a^+\rangle = \sin \vartheta \sin \phi |1\rangle + \cos \phi |3\rangle + \cos \vartheta \sin \phi |2\rangle \quad (1.23)$$

$$|a^-\rangle = \sin \vartheta \cos \phi |1\rangle - \sin \phi |3\rangle + \cos \vartheta \cos \phi |2\rangle \quad (1.24)$$

which are mixtures of bare states in the Λ -system. The states $|a^\pm\rangle$ are shifted by $\hbar\omega^\pm = \frac{\hbar}{2}(\Delta \pm \sqrt{\Delta^2 + \Omega_P^2 + \Omega_S^2})$ and are composed of mixture of all of the bare states. Since $|a^0\rangle$ has no contribution from $|3\rangle$, it is considered a dark state - atoms cannot be excited to state $|3\rangle$. It is the evolution of P and S fields that has an influence on whether atoms will be in state $|a^0\rangle$, $|a^\pm\rangle$ or a mixture [42]. Focusing on the dark state $|a^0\rangle$, we can introduce the mixing angle $\vartheta(t)$ defined as:

$$\tan \vartheta(t) = \Omega_P(t)/\Omega_S(t) \quad (1.25)$$

Now, manipulation of the angle ϑ directly influences the occupation only of states $|1\rangle$ and $|2\rangle$. Before the population transfer, $|a^0\rangle$ coincides with the $|1\rangle$ wavefunction by applying conditions corresponding to $\vartheta = 0$, thus for which $\Omega_P(t)/\Omega_S(t) \rightarrow 0$.

The transfer process to state $|2\rangle$ is complete when $|a^0\rangle$ coincides with $|2\rangle$. It means that the condition for the mixing angle value is $\vartheta = \pi/2$ and $\Omega_S(t)/\Omega_P(t) \rightarrow 0$. To transfer the population from state $|1\rangle$ to state $|2\rangle$, first the atoms should be exposed to the S pulse which couples unpopulated states. The P pulse begins before the S pulse fades. The envelope of pulses' intensity in time should be smooth, with no rapid variations, monotonously increasing in the first half and monotonously decreasing in the second half. A proper overlap of the two has to be ensured, to guarantee adiabatic evolution of the mixing angle. For the transfer to be adiabatic, the flow of population from state $|1\rangle$ to state $|2\rangle$ has to be gradual, only then state $|3\rangle$ does not become populated. This condition can be expressed with following inequality [43]:

$$\Omega_{\text{rms}} \gg |\dot{\vartheta}| = \frac{|\Omega_S(t)\dot{\Omega}_P(t) - \Omega_P(t)\dot{\Omega}_S(t)|}{\Omega_P^2 + \Omega_S^2} \quad (1.26)$$

where Ω_{rms} is defined as: $\Omega_{\text{rms}}(t) = \sqrt{\Omega_P(t)^2 + \Omega_S(t)^2}$.

Diagrams in Figure 1.7 depict the STIRAP procedure. First, the S pulse is released what can be seen on the diagram as Rabi frequency change. As the second pulse P begins to propagate with some delay relative to the S pulse, the mixing angle rises. Population transfer follows the mixing angle change, atoms from state $|1\rangle$ are transferred to state $|2\rangle$ while state $|3\rangle$ does not become populated. As the pulses fade, the mixing angle ultimately reaches $\pi/2$ and the transfer is completed.

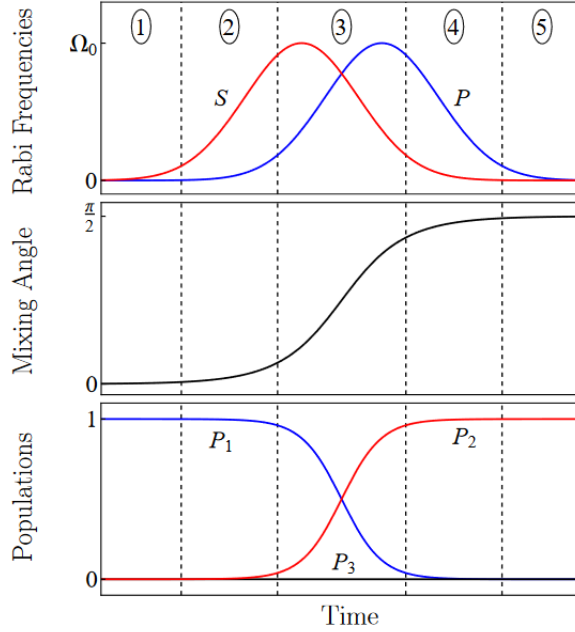


Figure 1.7: Diagrams showing key parameters' changes in the STIRAP process. First, the S pulse is applied and then, the P pulse is released such that the two overlap. The mixing angle changes smoothly from 0 to $\pi/2$ and the population is transferred from state $|1\rangle$ to state $|2\rangle$. Picture taken from taken from [43].

1.4.3. Electromagnetically induced transparency

The Hamiltonian in the electromagnetically induced transparency phenomenon considerations in a three-level lambda system is the same as in (1.19). This system, like in Figure 1.6, is also interacting with two light fields S and P. In EIT, the light fields differ in intensity with S field being stronger - pump and field P being weaker - probe. In EIT, unlike in STIRAP, the Ω_P/Ω_S ratio stays constant during the experiment.

A simulation of EIT is presented in Figure 1.8 and shows the populations in all of three bare states in a Λ -system while the pump beam detuning Δ_S is equal to zero and the frequency of probe field is scanned. We can imagine that the stronger pump beam depletes population of state $|2\rangle$ while the weaker probe pumps it back. We would expect, that when the probe's detuning Δ_P is zero, more atoms are pumped from state $|1\rangle$ to state $|2\rangle$ but we see population loss in state $|2\rangle$ instead. This behaviour is observed in so-called transparency region characteristic for EIT. Within it, the probe beam does not get absorbed by atoms and at $\Delta = 0$ condition, it is fully transmitted through an atomic cloud. It is a pure quantum effect - solving the Hamiltonian for $\Delta = 0$ results in obtaining zero probability amplitudes for population transfer from state $|1\rangle$ to state $|2\rangle$ [42].

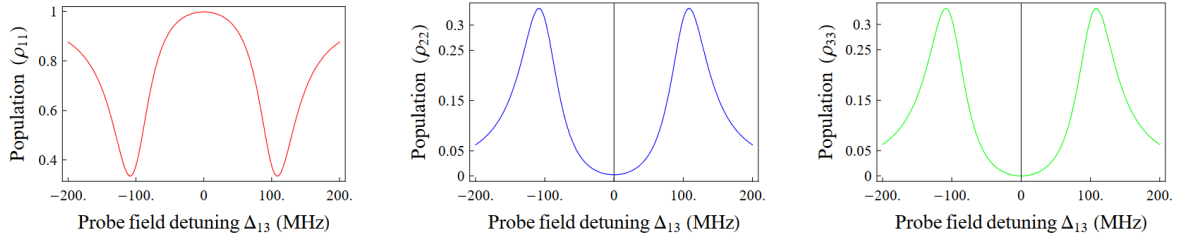


Figure 1.8: Simulation of the electromagnetically induced transparency. Δ_{13} is the probe beam detuning, $\rho_{11}, \rho_{22}, \rho_{33}$ are the diagonal elements of the density matrix of the system which are proportional to the corresponding levels' populations. In the simulation, pump beam is resonant with the transition, pump beam detuning is equal to zero, and probe beam frequency is scanned. Picture taken from [44].

Chapter 2

Cesium laser systems

This chapter details the construction of laser systems which use optical injection locking technique and which generate phase coherent fields with a frequency difference tunable around the cesium ground state hyperfine splitting, 9.192 GHz. Two related implementations are presented, each optimized for a specific application: Λ -enhanced gray molasses cooling, STIRAP and observation of electromagnetically induced transparency.

In section 2.1, we describe the setup prepared for Λ -enhanced gray molasses cooling experiment, in which a slave laser is injection locked to an EOM sideband.

Later in section 2.2, we will present the laser system built to perform STIRAP and EIT experiments in cold cesium atoms and the operation of the acousto-optical modulator and its performance in double-pass will be described. It will also outline light pulse preparation procedure. It consists of description of the light frequency and amplitude manipulation with AOMs and the electronics used for their control.

In the last part, section 2.3, we will characterize injection locking via Fabry-Perot cavity and optical beat-notes measurements.

2.1. Laser system preparation for Λ -enhanced gray molasses

Λ -enhanced gray molasses cooling requires phase coherent cooling and repumping beams. In this chapter we will show how to achieve them with a slave laser injection locked to a sideband generated in an EOM. For this reason, we begin by giving some more insight into the EOM's operation. Later, we will proceed with the description of the experimental setup for Λ -GMC and its operation.

2.1.1. Electro-optical modulator

An electro-optical modulator allows for light phase-modulation without introducing changes in its polarization and intensity [45]. It consists of a non-centrosymmetric crystal with two electrodes attached to its opposing sides. While the voltage is applied to them, refractive index of the crystal changes in a non-isotropic manner. In linear electro-optical effect the refractive index changes linearly with the applied electric field. In a transverse configuration of an electro-optical modulator (Fig. 2.1) which will be considered here, the electrodes are attached at crystal sides that are transverse to the light propagation axis. The electric field of the input light can be defined as:

$$E_{i_x}(t) = E_i \cos \omega t \quad (2.1)$$

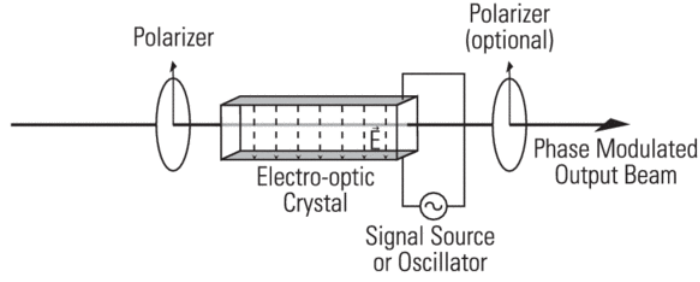


Figure 2.1: Scheme of an electro-optical phase modulator. The carrier wave passes through a polarizer and enters the electro-optical crystal. Electrodes are attached to the sides of the crystal and voltage is applied to them. Picture taken from [46]

where x' is the polarization axis of the input polarizer, E_i is the electric field's amplitude and ω is the input light frequency. The output light is phase-shifted:

$$E_o(t) = E_i \cos(\omega t - \phi) \quad (2.2)$$

where:

$$\phi = \frac{2\pi}{\lambda}(n_{x'} + \Delta n_{x'})L = \phi_o + \Delta\phi_{x'} \quad (2.3)$$

is the total phase shift which consists of two terms, $\phi_o = (2\pi/\lambda)Ln_{x'}$, where $n_{x'}$ is the unperturbed refractive index of the crystal in the x' direction λ is the input light wavelength and L is the crystal's length along the light propagation direction. It is simply a phase that accumulates when the light passes through a medium. The other term is $\Delta\phi_{x'} = \frac{\pi}{\lambda}L\Delta n_{x'}$, which is proportional to the refractive index change along the x' axis, $\Delta n_{x'}$. This change is dependent on the applied electric field \mathcal{E} , $\Delta n_{x'} \approx \frac{1}{2}n_{x'}^3 r \mathcal{E}$, with r being the electro-optical coefficient. The applied electric field's amplitude is $\mathcal{E} = V/d$. It depends on the applied voltage V and the distance between electrodes d . When the applied voltage is sinusoidal, the electric field will also be a sinusoidal signal $\mathcal{E} = \mathcal{E}_m \sin(\omega_m t)$ with an amplitude \mathcal{E}_m and modulation frequency ω_m . The electric field of the output light then becomes [45]:

$$E_o(t) = E_i [J_0(\delta) \cos \omega t + J_1(\delta) \cos(\omega + \omega_m)t - J_1(\delta) \cos(\omega - \omega_m)t + J_2(\delta) \cos(\omega + 2\omega_m)t - J_2(\delta) \cos(\omega - 2\omega_m)t + \dots] \quad (2.4)$$

where J_i are Bessel functions of i th order and $\delta = \frac{\pi}{\lambda}n_{x'}^3 r \mathcal{E} L$ being the phase modulation index.

In our experiment we used NIR-MPX800 fiber electro-optical modulator from iXblue. It is designed to operate in 780-890 nm wavelength range and with modulation frequencies up to 12 GHz. We operated it with 852 nm light and modulation frequencies around 9 GHz. Transmission through the device is 40%.

The RF modulation signal was generated by ADF5356 evaluation board (Analog Devices). While generating frequency around 9 GHz, the evaluation board have a bias of +170 kHz and it should be taken into consideration when setting the desired frequency in the board's software. It was also noticed that the generated signal was continuously fluctuating with few hundred Hz walk-off. Power of the generated signal is at -3 dBm level which is too low for efficient modulation in the EOM. Hence, it was amplified with one of the two amplifiers

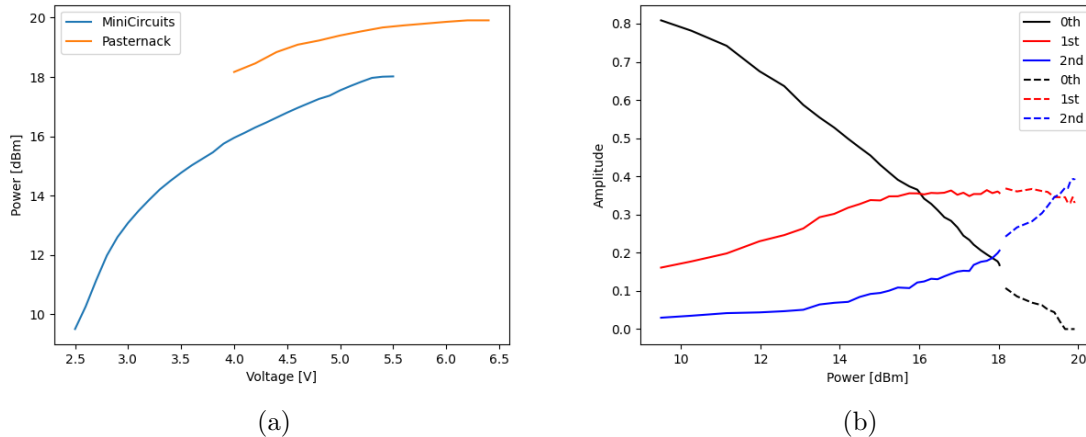


Figure 2.2: a) The power of the ADF5356 RF signal at 9.2 GHz amplified by an amplifier from MiniCircuits (blue line) and a Pasternack amplifier (orange line). b) 0th, 1st and 2nd sideband contribution in the 9.2 GHz EOM-modulated light spectrum. The amplitude is measured as a ratio of the sideband’s peak height to carrier wave peak height when light is not modulated. Solid lines represent measurements for which MiniCircuits amplifier was used, while the dotted lines represent measurements with Pasternack amplifier.

available in the laboratory that worked in this frequency range, ZX60-183A-S+ from MiniCircuits and PE15A4013 from Pasternack. By changing their supply voltage, we could alter the effective amplification as shown in Figure 2.2a for 9.2 GHz modulation signal.

The light modulated in the EOM was later sent to the Fabry-Perot cavity for spectral characterization. The amplitudes of the carrier (0th order) and the 1st and 2nd order sidebands were measured for different modulation signal powers at 9.2 GHz. The results are shown in Figure 2.2b.

2.1.2. Laser system operation

Cesium atomic levels scheme with the light frequencies of laser sources available in our laboratory and the frequencies required for Λ -enhanced gray molasses cooling (Λ_{GMC}) is presented in Figure 2.3. Both cooler master laser and repumper laser are external cavity diode lasers (DLpro, Toptica). The cooler master laser is offset-frequency locked to the $F=4 \rightarrow F'=4$ transition, while the repumper is locked directly to the $F=3 \rightarrow F'=3$ transition. Their frequency difference is equal to 8922 MHz and they are used as cooling and repumping beams in the magneto-optical trap and as sources for grey-molasses cooling beams. However, since they operate independently, they are not phase coherent.

In setup from Figure 2.4, repumper light source is replaced with output from slave laser SL1. This laser was built from commercial components with housing produced in the workshop available to our group. It is composed of a 852 nm Fabry-Perot, single mode laser diode (L852P100, Thorlabs) with up to 100 mW output. The assembled laser’s picture and its power vs. current characteristic is presented in Figure 2.5. This laser was injection locked with a +1st sideband generated in the EOM. The EOM’s input light was taken from the cooler master laser. By applying 8922 MHz modulation in the EOM and seeding SL1 with the +1st sideband it achieves the repumper laser frequency. At the same time, it also becomes phase coherent with the Thanks to injection locking it also becomes phase coherent

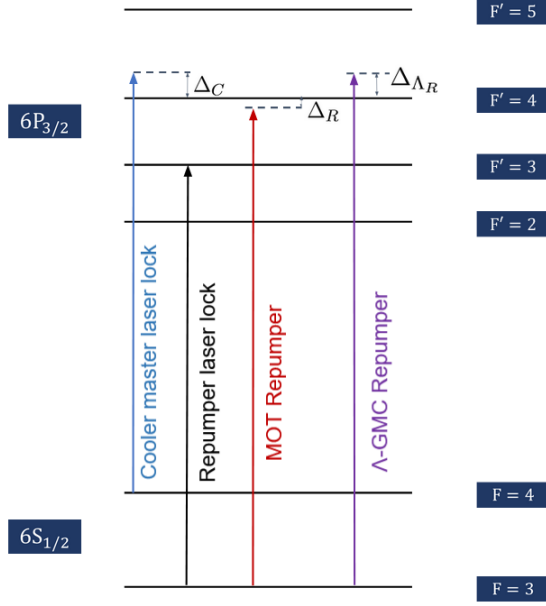


Figure 2.3: Atomic levels and light frequencies diagram for Λ_{GMC} experiment. The zero two-photon detuning condition is met when both Λ_{GMC} cooler and repumper detunings from $F'=4$ level are equal, $\Delta_{\Lambda_C} = \Delta_{\Lambda_R}$.

with the cooler master laser.

In the experiment with cold atoms, cooler master laser and SL1 injection locked to a sideband are used for generation of MOT beams, gray molasses cooling beams and Λ_{GMC} beams. Their distribution in the main experimental chamber is as for MOT configuration (Figure 1.1a). They are split into three pairs of counter propagating beams with orthogonal circular polarizations and illuminated on atomic cloud in Λ_{GMC} experiment.

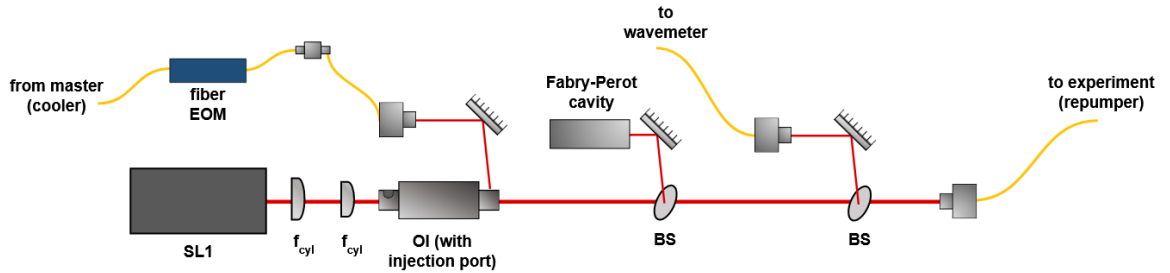


Figure 2.4: Λ_{GMC} repumper laser beam generation. The SL1 is injection locked to the +1st EOM's sideband. The laser's light spectrum is examined with a Fabry-Perot cavity and a wavemeter reading. SL1 laser's light is coupled to a PM fiber with a linear polarization and send to the main experiment. BS - beam splitter, f_{cyl} - cylindrical lens.

As shown in Figure 2.4, the seeding light was supplied to the SL1 laser diode's cavity through a special port in the optical isolator (IO-3-850-HP, Thorlabs), which gives access to the isolator's output Glen-Taylor calcite polarizer. Using beam splitters, a fraction of the slave's output light was sent to a Fabry-Perot cavity and a wavemeter for characterization.

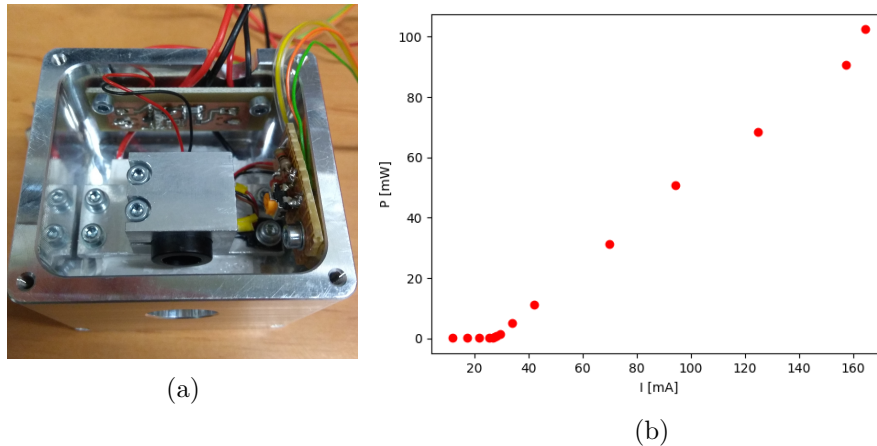


Figure 2.5: a) Assembled SL1 laser. b) Power vs. current characteristic of the SL1 laser diode. The laser action starts at 27 mA.

2.2. STIRAP and EIT experimental setup

2.2.1. Laser system

The experimental setup consists of two light sources which are phase coherent, a feature which is essential to successfully perform STIRAP. It is again obtained through the injection locking technique. A new SL2 laser is introduced into the setup. It is another semiconductor laser built with design analogous to SL1's. It consists of a Fabry-Perot single mode laser diode which can generate up to 150 mW of optical power (L852P150, Thorlabs). Its threshold current is 25 mA and its power vs. current characteristic is shown in 2.6. Two slave lasers SL1 and SL2 are seeded with light from one ECDL master laser stabilized to an atomic transition. The challenge is to obtain light fields which are detuned from each other by the value of the frequency difference between two hyperfine ground states of cesium, which is 9.192 631 770 GHz [26]. It is done through injection locking SL1 laser to a +1 sideband of master laser's light passing through an electro-optical modulator while the SL2 laser is injection locked with light coming directly from the master laser. The setup is shown in Figure 2.7. The master laser's frequency is detuned by +69 MHz from the $F=4 \rightarrow F'=4$ transition on the D2 cesium line. The frequencies applied to AOMs in double-pass configuration and to the EOM are such that the light from SL1 is tuned to the $3 \rightarrow 3$ transition while the SL2 light is tuned to the $4 \rightarrow 3$ as shown in Figure 2.8.

The experimental setup presented in Figure 2.7 is built for generation and characterization of light pulses generated from a phase coherent light sources. The SL1 laser is seeded with a +1 EOM sideband of master laser light sent through a port of an optical isolator or light from the EOM is directly sent to the optical setup entering through a polarization beam splitter, PBS2 placed behind the optical isolator. It can be decided whether EOM light is used for injection locking or it is sent directly to the system by changing its polarization right behind the EOM output so its power is either reflected or transmitted through PBS1. The SL2 laser is seeded with light coming directly from the master. Both output beams from SL1 and SL2 are shaped with two cylindrical lenses to increase efficiency of passing through OI and to make the beams more symmetrical. The SL1 or EOM output is later shifted by -220 MHz by a double-pass through AOM, while the SL2 frequency is shifted by -270 MHz

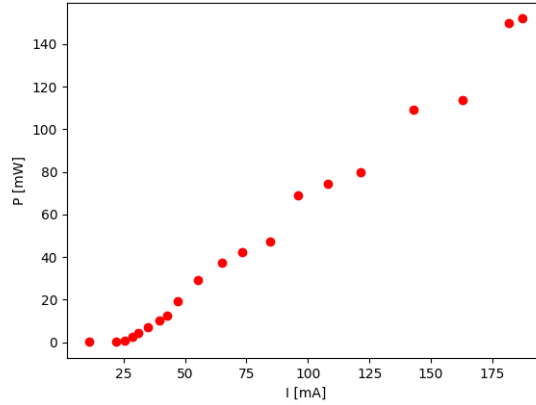


Figure 2.6: Power vs. current characteristic of the SL2 laser diode.

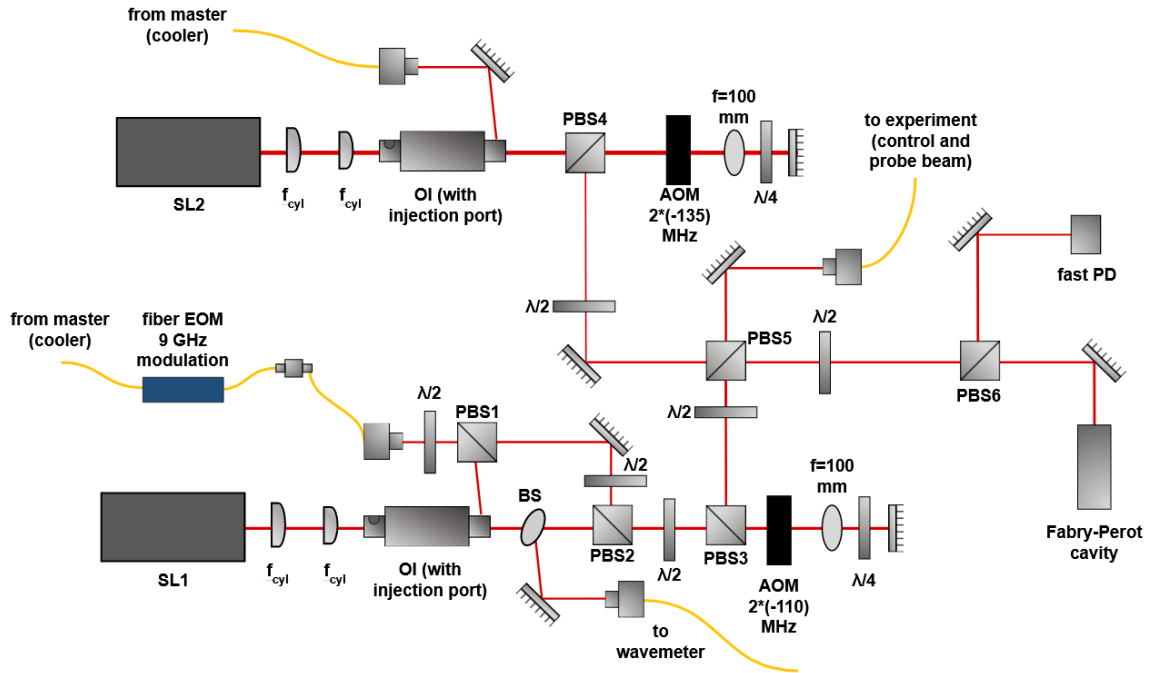


Figure 2.7: Scheme of optical setup for generation of phase coherent laser beams for STIRAP and EIT experiments. OI - optical isolator, PBS - polarizing beam splitter, BS - beam splitter, PD - photodiode, $\lambda/2$ - half-wave phase retardation plate, $\lambda/4$ - quarter-wave phase retardation plate, f_{cyl} - cylindrical lens.

also in a double-pass AOM configuration. After frequency shift, the beams are overlapped on PBS5 and then their polarizations are projected onto the same axis with use of PBS5. The overlapped beams are later sent to the Fabry-Perot cavity, onto the fast photodiode and coupled to an optical fiber to be sent to the experiment.

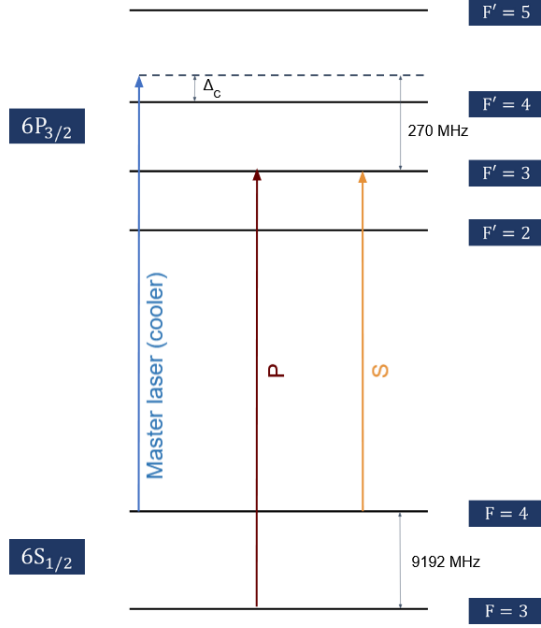


Figure 2.8: Diagram of light frequencies used and generated in the laser setup for STIRAP and EIT. Master laser's light is used for seeding and it is detuned by Δ_C from the $F=4 \rightarrow F'=4$ transition. P and S light frequencies are generated in the setup.

2.2.2. Acousto-optical modulator

A scheme of an acousto-optical modulator is shown in Figure 2.9a. It consists of a transparent crystal and a piezoelectric element supplied with an RF signal that causes vibrations of the crystal. An optical beam incident on the crystal travels through a created acoustic wave. The acoustic wave causes spatial modulation of the refractive index which causes Bragg diffraction of the optical beam. Occurring Bragg diffraction is characterized by the Bragg angle θ given by the equation:

$$\sin \theta = \frac{\lambda f}{v} \quad (2.5)$$

where λ is light's frequency in air, f is acoustic wave's frequency and v is its propagation velocity. The optical waves are effectively reflected from the moving acoustic planes and they are frequency shifted according to the Doppler theory [47]. Under modulation with sinusoidal signal, the light passing through an AOM will be scattered mostly to the ± 1 st diffraction orders with resulting frequencies:

$$\nu = \nu_0 [1 \pm 2n \cdot v \cdot \sin(\theta/2)/c] \quad (2.6)$$

where ν_0 is the input light frequency, n is the refractive index of the crystal and c is the light velocity. However, also higher diffraction orders can appear with frequencies $\nu = \nu_0 [1 \pm 2mnv \sin(\theta/2)/c]$ and deflected with an angle following relation $\sin \theta = m\lambda f/v$, where m is the diffraction order.

The efficiency of light scattering into a defined diffraction order can be optimized by adjusting the power of the RF signal supplied to the piezoelectric transducer and by adjusting modulator's position and angle relative to the optical axis. In our setup we use AOMs in a double pass configuration, as presented in Fig. 2.9b. In the double pass, the light first

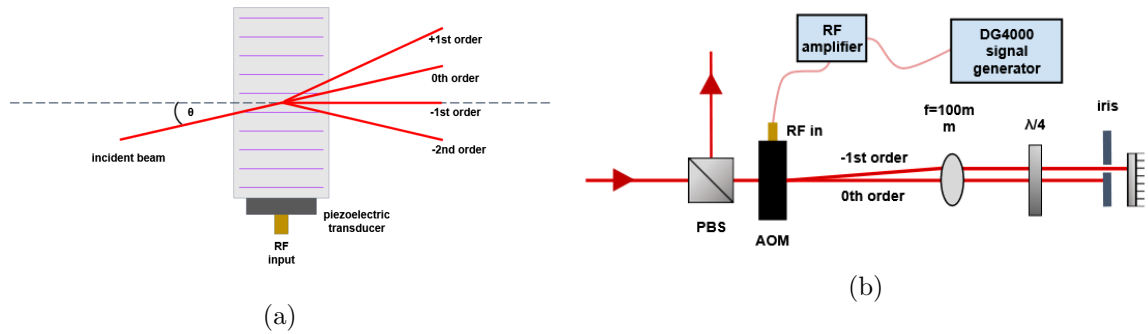


Figure 2.9: a) Acousto-optical modulator operation. The RF signal applied to a piezoelectric transducer causes the crystal to vibrate and acoustic waves are created along it. The light passing through the crystal scatters from the density pattern in the crystal which experiences periodic changes of the refractive index due to expansion and compression caused by the acoustic waves. The light can be scattered into several diffraction orders. b) AOM in double pass configuration. PBS - polarization beam splitter, λ - quarter-wave phase retardation plate. RF signal is generated with Rigol DG4000, amplified with an RF amplifier and supplied to the AOM.

passes through an AOM with a certain linear polarization and is optimized for maximum -1st order diffraction efficiency. Then, a lens is placed in a $2f$ configuration such that the beam is focused on the mirror and become collimated again after passing the lens on the way back. The quarter-wave phase retardation plate ensures that the light is rotated in total by 90° so it can be separated from the incoming beam a polarization beam splitter. Only the -1st order is reflected to go through the AOM again other diffracted beams are blocked with an iris. It is to ensure that no unwanted light components leak into the double-pass output beam, e.g. double 0th diffraction order pass which would be overlapped with double -1st diffraction order pass path.

2.2.3. Generation of optical pulses

STIRAP requires that the cold atoms cloud is illuminated with two light pulses of a specified frequency. The light sent to the experiment is modulated with AOMs. Varying power of RF signal applied to the AOM will also vary light amplitude at its output. As shown schematically in Figure 2.9b, the acousto-optical modulators in our setup are supplied with signal generated by Rigol DG4000 which was later amplified with a RF amplifier. The efficiency curves for AOMs in double pass used in the experimental setup are shown in Figure 2.10a - dependence on RF power, the variable is peak-to-peak voltage of signal generated with DG4000 and Figure 2.10b - dependence on the modulation frequency. From the curves, we see that the dependence of light amplitude on the RF power is not linear. It implies that in order to obtain a light pulse of desired shape, the non-linear RF amplification effects have to be taken into consideration for proper calibration.

The double pass efficiency curve is an increasing and monotonous function of the signal generator's voltage reading and it eventually reaching a plateau. The efficiency vs. voltage dependency was later reversed and a 12th-order polynomial was fitted to the voltage as a function of normalized efficiency as shown in Figure 2.11. A polynomial found with this approach was used as a function converting an arbitrary pulse shape function to the signal generator's signal that has to be applied at the output to reproduce the pulse. An example

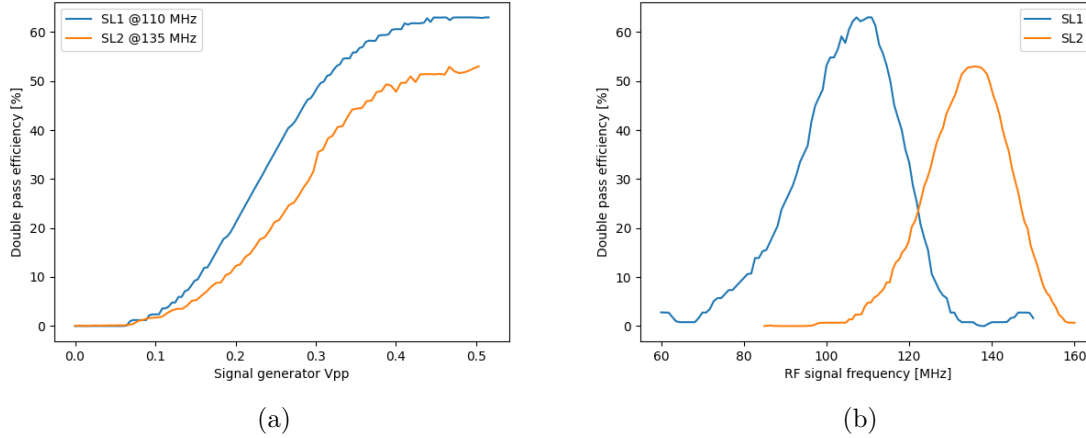


Figure 2.10: a) AOM double-pass efficiency for SL1 beam for AOM operating at 110 MHz, 2x-1st diffraction order (blue line) and for SL2 beam with AOM operating at 135 MHz, 2x-1st diffraction order (orange line) as a function of signal generator output sine function peak-to-peak voltage (V_{pp}). b) AOM double-pass efficiency as a function of the RF signal frequency applied to the modulator, 2x-1st order, SL1 - blue line, SL2 - orange line.

is shown in Figure 2.11b, where a Gaussian envelope is converted into the signal generator output sequence with voltage normalized to V_{max} .

The DG4000 Rigol signal generator was used because of its multiple options for signal generation and possibility of external and automated control. One of the generator's commands allow for saving an arbitrary signal function in its volatile memory. Since it has two output channels, one of them was used for generations of the P pulse and the other one for generation of the S STIRAP pulse. Once the pulse shapes were saved in the device's memory, both channels were set to external trigger burst mode, which allows for generating a defined function with N-cycles repetition which is released when high signal is applied to the trigger channel. In case of the STIRAP Gaussian pulses, they have to be single pulses, thus in our case $N=1$. Since both channels were supplied with the same trigger signal, one of the pulses has a programmed delay relative to the other pulse. The time delay between pulses burst from the channels can be arbitrarily chosen and controlled externally.

The volatile memory of each channel has a capacity to store no more than $M=16384$ input values between -1 and 1 in a sequence. The values are later scaled with the voltage U set at the channel output, so they can be programmed to be between $-U$ and U . Later, a period T of such a pulse is defined and the sequence is spread within the period outputting consecutive points with M/T rate.

The important issue is that the burst mode of DG4000 does not allow for simultaneous frequency modulation of the pulse saved in volatile memory, so the sequence saved in the device already has to be multiplied by a sine function. The central frequencies (f_c) of AOMs operation are 110 MHz for SL1 path and 135 MHz for SL2 path. Hence, the desired pulse shape envelope was first multiplied by sine and only then transformed to a voltage sequence that should be outputted from the signal generator. Because only 16384 points could be saved in one channel's volatile memory, the generated pulses cannot have arbitrarily long duration because of insufficient sine probing. Number of points per one period of sine for the AOMs' central frequencies is presented in Table 2.1. With insufficient probing, the sine function will not be well reconstructed and it will introduce frequency artefacts or cause signal amplitude

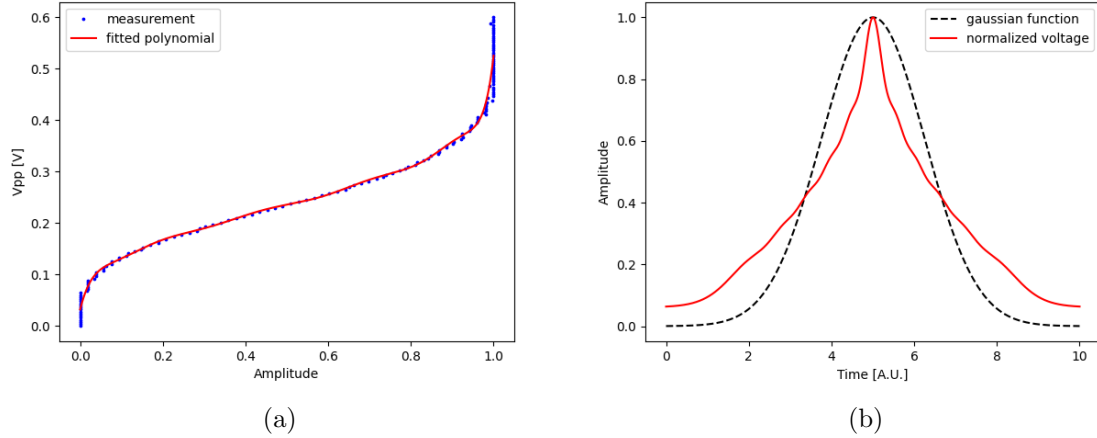


Figure 2.11: a) Measurement (blue dots) and 12th order polynomial function fitted (red line) to the peak-to-peak voltage of the sine function generated by Rigol DG4000 as a function of normalized efficiency (amplitude equals 1 for maximum double pass efficiency of the SL1 laser beam). b) Gaussian function with amplitude equal to 1 (black dashed line) and a function shape to be outputted from the signal generator to reproduce the Gaussian shape (red curve) normalized to the V_{max} , a value for which signal amplitude is equal to 1.

decrease.

Table 2.1: Sampling of sine with 110 MHz and 135 MHz for different pulse durations. The higher the frequency the lower the sampling, meaning less points per one period of sine function.

f [MHz] \ t [μs]	5	10	15	20	25	30
110	29.8	14.9	9.9	7.5	6.0	5.0
135	24.3	12.1	8.1	6.1	4.9	4.0

The pulse generation system was tested for Gaussian shaped output:

$$A = \exp(-(t - \tau)^2 / (2\sigma^2)) \quad (2.7)$$

where A is signal amplitude, t is time, τ is the time for which Gaussian is maximal and σ^2 is its variance. In the test, the pulse's duration t_p was defined to last 6σ with $\tau = t_d$. The results showing measured amplitudes and fitted Gaussians for pulses of different durations are shown in Figure 2.12. The relative amplitude of the pulses compared to the amplitude of light when AOM is supplied with continuous sinusoidal signal is lower than 1. It means that the efficiency of μ s order pulses generation is lower than continuous operation. We would expect, that the longer the pulse's duration, the lower their amplitude due to insufficient sampling. This is more visible for the pulses generated with AOM whose working frequency is 135 MHz since the sine modulation period is shorter and it is sampled with less points.

Also, the fitted Gaussian functions have smaller σ parameters than the set values, what can be seen in Figure 2.13. However, it is easy to balance pulse's duration by proper scaling in the control system.

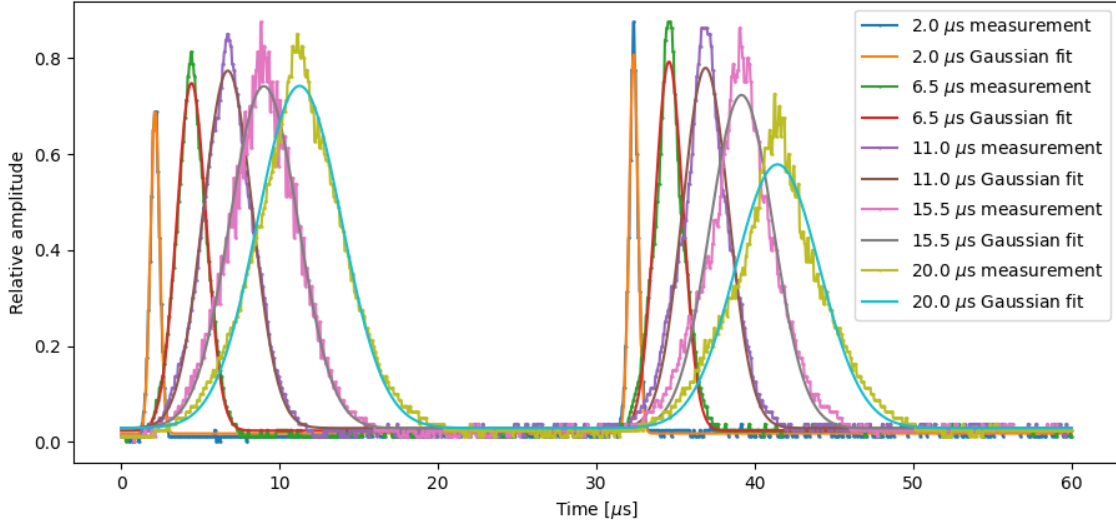


Figure 2.12: The resultant Gaussian pulses. The left-hand side Gaussian shape is obtained with the SL1 light, while the right-hand side Gaussian is obtained with the SL2 light. Both pulses' light paths were spatially-overlapped and observed on the same photodiode. Times in the legend correspond to the set pulse duration. The delay between bursting SL1 and SL2 pulses was set to $30\ \mu\text{s}$. The relative amplitude on the y-axis is measured as signal ratio compared to the AOM's output when signal generator's output was a continuous sinusoidal function with optimal peak-to-peak voltage.

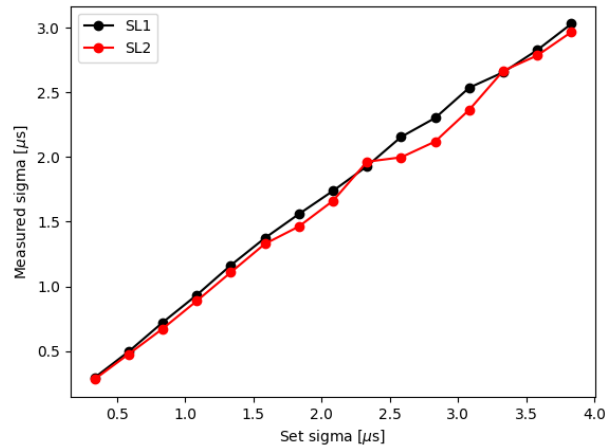


Figure 2.13: The dependence of measured pulse width sigma obtained by fitting a Gaussian function to the shaped pulse on the pulse width that was set originally. The measured width is on average 82% of the set one which means that the pulses are compressed in the system.

The system was also tested for generation of other shapes including square pulses which will be later used in the electromagnetically-induced transparency experiment.

2.3. Injection locking of cesium lasers

For two optical signals with E_1 and ω being the amplitude and frequency of the first optical field, E_2 being the amplitude of the second optical field, Δ being its frequency difference from the first one and ϕ being phase difference.

$$E(t) = E_1 \exp(i\omega t) + E_2 \exp(i((\omega + \Delta)t + \phi)) \quad (2.8)$$

The beat notes signal for these two fields is:

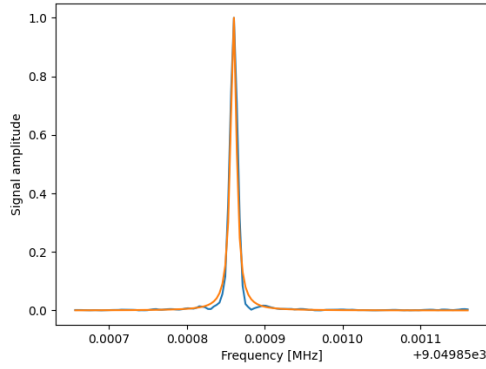
$$E(t) = |E_1|^2 + |E_2|^2 + 2E_1E_2 \cos(\Delta t + \phi) \quad (2.9)$$

with its time-varying part having frequency Δ . Spectrum of the beat-notes signal can be observed with a spectrum analyser and its width is dependent on the time variations of Δ and ϕ . If the frequency difference between two light sources is well-defined, phase-fluctuation can be characterized as its variation will cause beat-notes spectrum broadening.

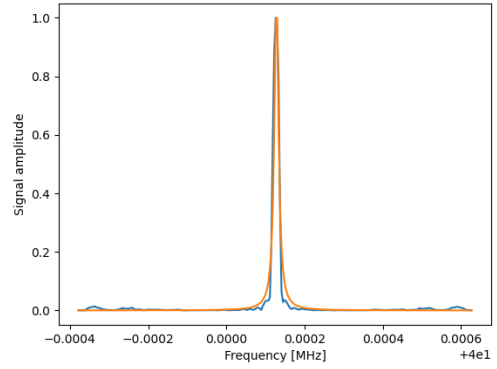
The beat notes between SL1 and SL2 lasers were measured on a fast photodiode with the optical setup shown in Figure 2.7. They were spatially overlapped with each other, they both had the same linear polarization and were focused on the photodiode's detector. The beat-notes measurements are presented in Figure 2.14.

Several parameters were changed from one measurement to another: seeding light sources for SL1 and SL2 lasers were either coherent or incoherent, SL1 was either seeded with light that was or was not modulated by the EOM and the frequencies used in AOMs double pass configuration influenced frequency shifts between the SL1 and SL2 light beams. Measurements a) and b) were taken when both SL1 and SL2 were seeded with light sourcing from one external cavity diode laser stabilized to an atomic transition. In a) SL1 is injection locked to +1st EOM sideband detuned 9 GHz from the carrier and additional frequency difference of 50 MHz was generated by the AOMs in the system. In b) SL1's seeding light was not modulated in the EOM so only 40 MHz frequency difference is introduced by AOMs. When the seeding light is modulated with the EOM, the bandwidth of the beat-notes signal is 91.1 Hz, more than 26.5 Hz for the case with unmodulated seeding light, what implies that the coherence between two beams is better preserved in the latter. Measurements c) and d) were performed with two independent seeding light sources being the same ECDL models, both locked to an atomic transition and detuned from each other by 8892 MHz. In measurement c) the seeding light for SL1 is not modulated with the EOM while in d) SL1 is injection locked to the +1st sideband detuned from the carrier frequency by 8892 MHz. In both of these measurements, additional frequency difference of 50 MHz is caused by the AOMs. The beat-notes signal worsened significantly for independent seeders and the bandwidths are 2.2 MHz for c) and 2.1 MHz for d). These values are five orders of magnitude higher than for the case with one seeding light source.

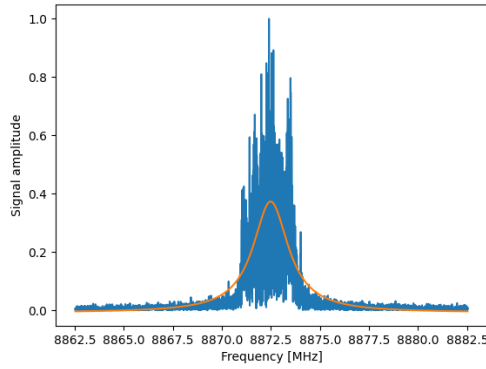
Figure 2.15 shows spectrum of the SL1 laser when it is injection locked to a +1st sideband of cooler master laser lock frequency modulated in the EOM with 18.4 dBm of 8886.4 MHz RF signal applied to it. The measurement in the Fabry-Perot cavity shows that the laser's operation is multimode. By manipulating modulation signal's power, we were able to distinguish components of light corresponding to the existing modes. A function consisting of sum of four lorentzians was fitted to the measurement result and the contribution of each resolvable mode was calculated by integrating each lorentzian separately. It was calculated that the percentage contributions of the modes are: 9% of one of the 2nd order sidebands frequency, 12.4% of the -1st sideband frequency, 4.5% of the carrier wave frequency and 74.1% of the desired frequency corresponding to the +1st sideband. As EOM characteristic



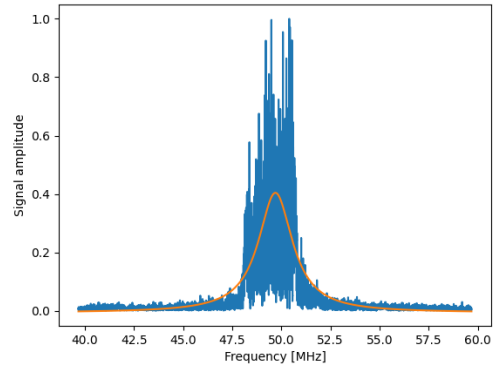
(a) FWHM = 91.1 Hz



(b) FWHM = 26.5 Hz



(c) FWHM = 2.2 MHz



(d) FWHM = 2.1 MHz

Figure 2.14: Beat-notes between SL1 and SL2 lasers seeded with light coming from the same master laser - a), b) and from different master lasers - c), d). Blue line - measured signal, orange line - fitted lorentzian. FWHM values are obtained from lorentzian fitting. a) SL1 seeded with +1st EOM sideband and SL2 seeded with light coming directly from the master laser. b) Both SL1 and SL2 are seeded with unmodulated master laser light. c) SL1 and SL2 seeded with independent master lasers with frequency difference of 8922 MHz. d) SL1 seeded with +1st sideband generated from first master light and SL2 seeded with second master laser light. In b) the measurement is limited by 30 Hz resolution of the spectrum analyzer.

in Figure 2.2b shows, for the power of RF signal applied, the carrier wave was still present at the EOM output and made up about 7% of its total power. It would be preferable to suppress the carrier completely by applying higher RF signal power to the EOM since its presence might cause undesired transitions in the performed experiments. However, by doing that we also increase the share of higher order sidebands competing with the +1st one, what led to unstable operation of the SL1 laser.

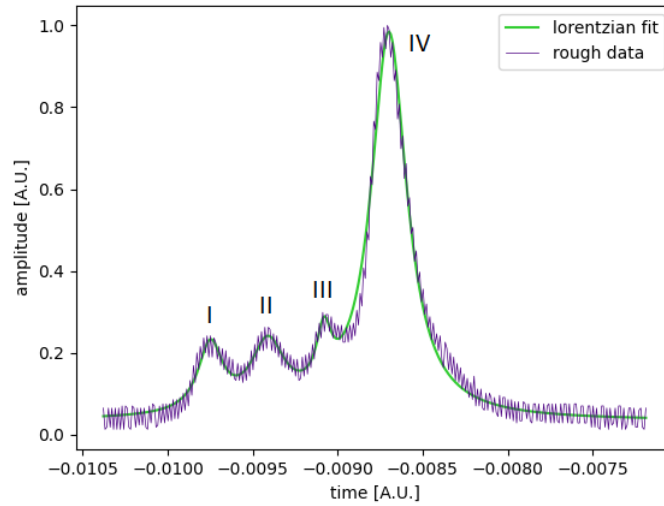


Figure 2.15: Spectrum of the SL1 repumper laser injection locked to the +1st sideband of the EOM supplied with 8886.4 MHz RF signal observed in a Fabry-Perot cavity (violet). The peaks are contributions from I - some 2nd order sideband, II - -1st sideband, III - 0th sideband, IV - +1st sideband. A function consisting of four lorentzians (green) was fitted to the measured spectrum.

Chapter 3

All-fiber 1064 nm laser module

This chapter will be devoted to a 1064 nm laser system which also uses this method of injection locking. The 1064 nm laser module and its components will be described. The module was designed to be a mobile all-fiber device operating with fiber components for beam splitting and optical isolation. Its simple design is embedded into an aluminum housing. The laser is composed of a Fabry-Perot commercial laser diode which is seeded with a master fiber laser's light delivered to the slave's laser diode cavity with a fiber optical isolator. What is more, the master laser can be integrated with the slave laser module making it a compact system and mobile.

Optical injection locking via an optical circulator was reported only twice up to date [48], [49]. In 2015, group from Berkley performed used this technique to injection lock a 1.55 μm vertical cavity surface emitting lasers and in 2018, group from Yale used it to injection lock of a a fiber-pigtailed laser diode operating at 980 nm.

In the following section 3.1, some of the module's components crucial for its operation will be described. Then, in section 3.2, design and assembly of the module will be presented.

3.1. Fiber components

All of the fiber components used in this experiment are composed of polarization-maintaining (PM) single-mode fibers with FC/APC connectors. The polarization is maintained within the fiber by introducing stress birefringence. Two stress-applying rods are placed such that the core of the fiber lies between them. If the input light's polarization is aligned with the birefringence axis, the polarization does not vary even when pressure is applied to some part of the fiber.

- **Optical fiber splitters.** They combine two fibers which are fused and tapered. Their cores are very close to each other, causing light coupling from one fiber to another. The coupling ratio depends on the length L of the coupling region and on the proximity d of the two cores. Gaussian beam propagates mainly through fiber's core but an evanescent wave consisting of its tail propagates through the cladding. When another core is close enough, the energy is coupled there. Any splitting ratio can be achieved by terminating fusing process at the right point. The scheme of this so called fused biconical taper process [50] is shown in Figure 3.1.

- **Optical isolator** lets the light pass through in only one direction so it can be used to block the back-reflected light. It is composed of an input polarizer, a Faraday rotator and an output polarizer [51]. Faraday rotator consists of a transparent material susceptible to the Faraday effect and a surrounding magnet that creates magnetic field parallel to the light

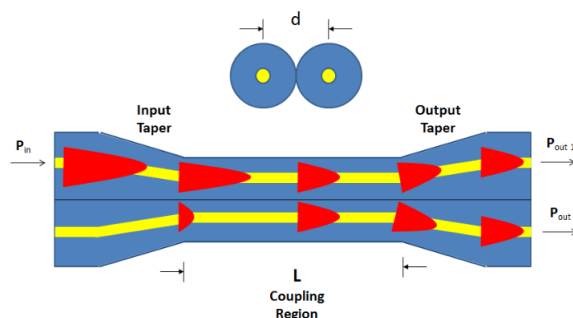


Figure 3.1: The fused biconical taper process. Light entering the input taper has power P_{in} . It propagates through a fiber fused with another one along the coupling region of length L . After fusing the fibers, their cores' separation is given by d . After the output taper, the light's power is split into P_{out1} and P_{out2} . Picture taken from [50].

propagation axis. When light passes through the rotator, its polarization plane is rotated by the angle $\theta = VBd$ proportional to the magnetic field B , material sample's thickness d and the Verdet constant V which is characteristic for the used material and characterizes strength of Faraday effect in this material. Angle θ and polarizers' orientations are chosen in such a way that the light can propagate in only one direction. It is a non-reciprocal device since the light's polarization plane rotation in back propagation adds up instead of canceling. The optical isolator can be incorporated in a device that has optical fiber input and output and fiber's key is then aligned with a specific fiber's axis so that the polarization plane of the light coupled to the fiber is aligned with the input polarizer's axis.

- **Optical fiber circulator** is composed of three ports through which the light propagates in non-reciprocal way. The light inputted at the 1st port passes to the second one, but the light inputted in the 2nd port does not reach 1st one. Instead, it propagates through the device to be outputted at the 3rd port. The structure of a fiber circulator is presented in Figure 3.2. First, light passes a birefringent crystal block which causes the ordinary and extraordinary rays to become spatially separated. Then, both beams undergo phase retardation while propagating through Faraday rotator and a phase-retardation plate and are incident on another birefringent crystal block. After passing the block, both rays are again overlapped and outputted at the second port. In the case of the backward propagation, the light inputted at the 2nd is again spatially split in a walk-off occurring in the birefringent crystal. Moving in this direction, rays' polarization is not affected by the phase retardation plate and the Faraday rotator since phase retardations that they introduce cancel each other out. Hence, when passing through the second crystal block, the extraordinary ray undergoes a second walk-off. Both rays can be combined with use of a reflection prism and a polarization beam splitter. However, in an all fiber design of the optical circulator, only one polarization is accepted at the inputs of the 1st and 2nd port so that its only the ordinary or extraordinary ray that can enter device's core. Beams propagating in opposite direction follow different paths so that the light circulates between ports. Such an optical isolator effectively suppresses any back reflections making it a good substitute for an optical isolator.

3.2. Design and assembly

The 1064 nm laser module is designed to fit in a mobile housing with built-in output ports 3.3. The housing is cut from a piece of aluminum with a separate lid and its total size is

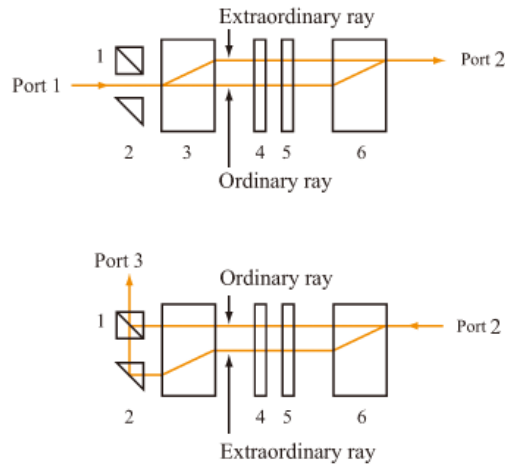


Figure 3.2: Fiber optical circulator working principle. The elements of the circulator are: 1 - polarization beam splitter, 2 - reflection prism, 3 - birefringent crystal, 4 - Faraday rotator, 5 - phase-retardation plate, 6 - birefringent crystal. The upper part shows ordinary and extraordinary rays' path from port 1 to port 2, while the lower part shows the rays' path from port 2 to port 3. Picture taken from [52].

25cm x 13cm x 7cm. The assembled module is presented in Figure 3.4a and its components are presented in Figure 3.5. It consists of a Fabry-Perot 1064 nm single mode laser diode (M9-A64-0300, Thorlabs) with 300 mW output power placed in a collimation tube which is mounted in an aluminum holder. The holder has a small hole in proximity with the collimation tube, where a 10 k Ω thermistor is placed. A Peltier module is placed under the aluminum collimation tube holder and together with the thermistor it is connected to a DLC Toptica current and temperature controller. The laser diode is powered by the same device in the constant current mode. The output power of the laser diode as a function of supplied current is shown in Figure 3.4b. The threshold current is 34 mA.

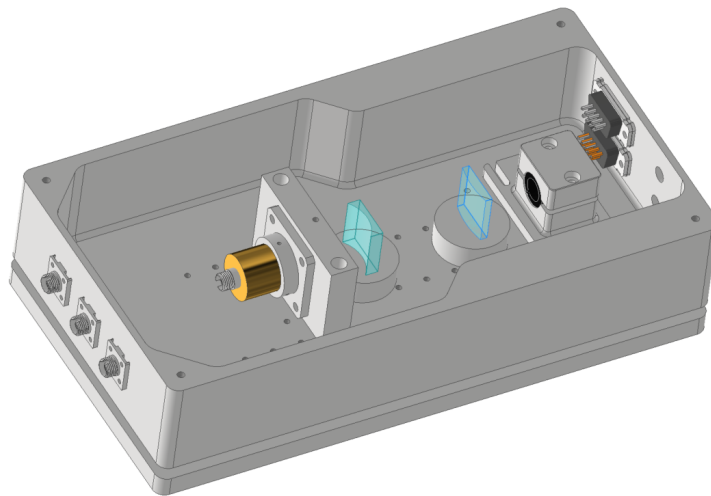
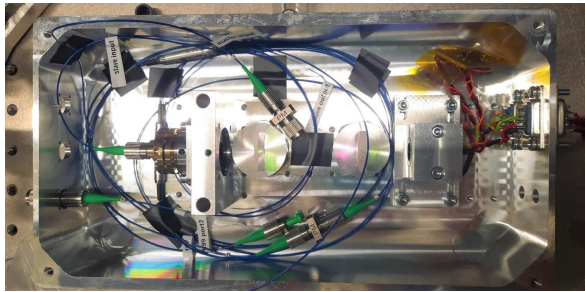
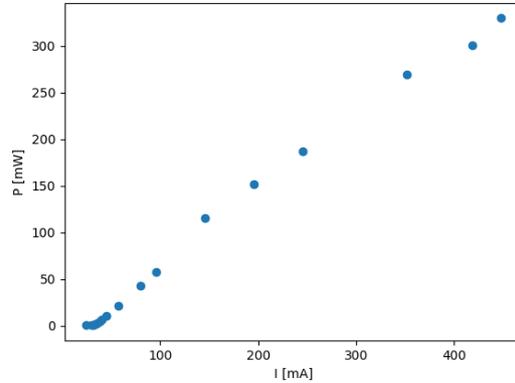


Figure 3.3: Design of the module prepared with a Computer-Aided Design software.



(a)



(b)

Figure 3.4: a) 1064 nm assembled module. Current and temperature controller is connected via D-sub9 connectors built in the module's wall on the right. The laser diode's output has common axis with the cylindrical lenses and the coupler. Light from the module can be outputted with additional fiber by connecting it to the beam splitter's output through one of the mating sleeves incorporated into the module's wall on the left. b) Output power in free-space vs. current characteristic for the slave 1064 nm laser diode. Lasing starts at 34 mA. The maximal power output is 330 mW at 448 mA for a free-space operation.

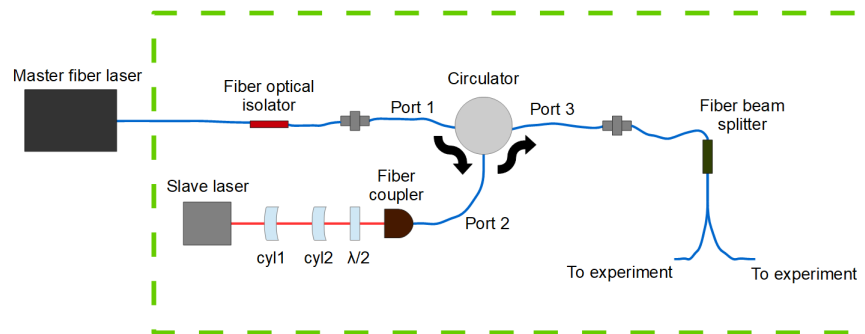


Figure 3.5: Setup built for injection locking of the 1064 nm laser diode with master fiber laser. Master's light passes through a fiber optical isolator to prevent back-reflections and then enters the 1st port of the optical circulator. It is outputted at the 2nd port and coupled to the laser diode's cavity. The slave laser's light is shaped with two cylindrical lenses and coupled to the 2nd port of the circulator and is outputted from the 3rd port. It is later split into a reference path for spectral characterization and a path to be used in the experiment. The elements within the green dashed line rectangle are within the aluminum package of the slave laser module.

Since the laser diode’s output beam is not Gaussian, only one axis is collimated with a lens placed in the collimation tube. The horizontal axis is shaped with two cylindrical lenses with $f=80$ mm and $f=-30$ mm which are glued inside the module. The light then passes through a half-wave retardation plate to align light’s polarization plane with the fiber axis and it is coupled to Port 2 (Figure 3.5) of an optical circulator with a 60SMS laser beam coupler (Shäfter + Kirchhoff) which has six degrees of freedom and allows for efficient on-axis coupling without additional mirrors. The obtained coupling efficiency is 51%.

The master 1064 nm single mode fiber laser (Rock Module, NP Photonics) is coupled to the first port of the circulator (CIR-PM-64-L-1-2, AWF Optics). A fiber optical isolator is placed between port one of the circulator and the master laser in order to block any back-reflections of the circulator as they influence master’s laser stability. The producer states that the Rock Module’s linewidth is below 5 kHz. Its output power is 15 mW and it was split with an optical fiber splitter so that its power at the output of the second port of the isolator used for seeding was 2.4 mW.

3.3. Performance

The 1064 nm slave laser injection locked to the master fiber laser was used to seed a fiber amplifier with maximum 50 W output from Azurlight Systems. The output beam of the amplifier was shifted by 110MHz in frequency with an acousto-optical modulator and overlapped first with the master light and later with the slave light to measure beat-notes signal on a photodiode. The measurements were made for equal powers of the beams between which the beat-notes were observed. The slave was operating at 103 mA and 31°C and the seeding light power was 2.4 mW.

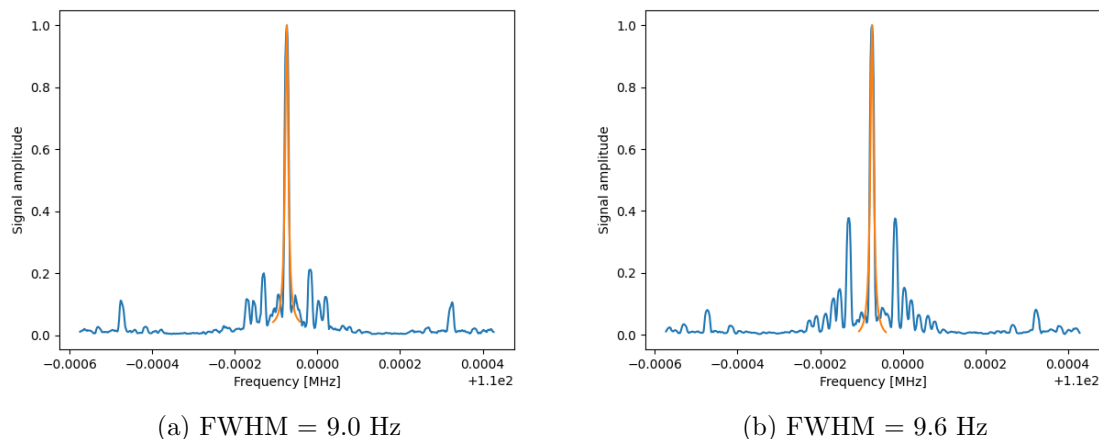


Figure 3.6: Beat-notes between amplifier seeded with slave laser’s light and a) master laser, b) slave laser. Blues line represents the measured spectrum and orange line is a lorentzian fit. FWHM values under the graphs were taken from the fitting parameters. The light from amplifier is detuned by 110MHz from the seeding light with an AOM. Beat-notes signal was normalized to its maximum. The measurements are limited by the spectrum analyzer 10 Hz resolution.

The beat-notes measurements are shown in Figure 3.6. Graph a) is a beat notes signal between the amplifier and master laser observed in a spectrum analyzer and its FWHM is

9.0 Hz. Graph b) is a beat notes signal between the amplifier and slave laser with 9.6 Hz FWHM. Beat-notes spectra with widths of this order imply that all of the three components - master laser, slave laser and master laser are phase coherent.

The output of master laser Rock Module is only 15 mW and it is currently used as a seeder for the Azurlight amplifier which is a source of light for a dipole trap [53]. Its output power is only enough to seed this one amplifier and its light cannot be used for other purposes. Usable output of the module when slave laser diode is injection locked to the master's light is about 160 mW, an order of magnitude more than master laser's output.

It was tested that with 5 mW of seeding light, the module could be injection locked almost continuously for every slave's current settings. It means, that we can obtain up to 160 mW of light at the optical circulator's output which would be phase coherent with the master. Assuming that two beam-splitters are used to split slave's light into one reference path (1% of the slave's output would be enough for this purpose) and two experimental paths, we would experience an average 25% loss of power. It means that the effective usable power on the two experimental paths could reach in total about 120 mW.

The slave laser could seed two 1064 nm optical amplifiers available in the laboratory, Nufern and previously mentioned Azurlight, both with maximum 50 W of output power. Since light from the amplifiers would be phase coherent, coherent addition [54] of the two beams could be performed in order to create a very bright light source.

Chapter 4

Observation of coherent phenomena

4.1. Λ -enhanced gray molasses cooling

In the Λ -enhanced gray molasses cooling (Λ_{GMC}) experiment, the repumper beam was generated with the SL1 laser injection locked to the +1st EOM sideband with the setup from Figure 2.4. The EOM was supplied with 18.4 dBm of 8926.4 MHz RF signal. The SL1 laser was operating at 170 mA and temperature was stabilized at 33.5 °C. It was seeded with 7.5 mW of EOM's output light. The cooler and repumper beams were detuned above $F'=4$ as presented in Figure 4.1 with acousto-optical modulators and frequency scans were possible for both of them. During the measurements, the Λ_{GMC} cooler was set at a constant frequency and Λ_{GMC} repumper was scanned.

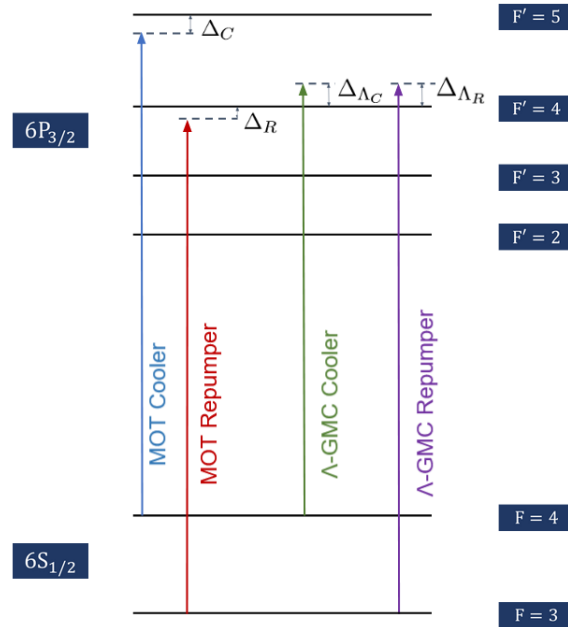


Figure 4.1: Cesium D2 line atomic levels and beams' frequencies diagram for Λ_{GMC} experiment. The zero two-photon detuning condition is met when both Λ_{GMC} cooler and repumper are detuned 29 MHz up from $F'=4$ level.

Experimental sequence performed to observe Λ -enhanced grey molasses cooling is shown in Table 4.1. First, cesium atoms were trapped in the magneto-optical trap, then the atomic

Table 4.1: Λ -enhanced gray molasses cooling sequence. Intensities are expressed in terms of the saturation intensity, $I_S = 1.65 \text{ mW/cm}^2$. CMOT - compressed magneto-optical trap, GMC - grey molasses cooling.

	B [G/cm]	I_C [I_S]	I_R [I_S]	Δ_C [MHz]	Δ_R [MHz]	Δ_{Λ_C} [MHz]	Δ_{Λ_R} [MHz]	T [μK]
MOT (5s)	15.1	14.7	0.9	-10.4	-6.4	-	-	230
CMOT (10ms)	31.1	14.7	0.9	-16.4	-12.4	-	-	-
GMC (25ms)	0	3.4	0.08	-	-	29.0	0	23
Λ_{GMC} (4ms)	0	1.6	0.06	-	-	29.0	29.0	6.3

cloud was compressed in a compressed magneto-optical trap (CMOT) stage and later cooled with grey molasses cooling down to $23 \mu\text{K}$. At that point, the magnetic field of the magneto-optical trap was off and cooling was continued with Λ_{GMC} scheme.

The Λ_{GMC} experiment was optimized for the lowest temperature and this was the parameter of interest, that is why the atom number consideration was omitted. We assume that the grey molasses cooling preserves number of atoms in the trap. The temperature optimization was done in several steps. First, the time of flight measurements were performed with Λ_{GMC} cooler detuning from $F = 3 \rightarrow F' = 4$ being $+29 \text{ MHz}$ and Λ_{GMC} repumper frequency being scanned around the zero two-photon detuning. In the time-of flight method, we measure directly σ_x , that is the sigma parameter of a Gaussian function fitted along the x-axis of the atomic cloud after a few milliseconds of free-fall. After releasing the cooled cloud of atoms, it expands due to the kinetic energy that the atoms possess. The greater the temperature, the greater the mean velocity of atoms, resulting from Maxwell-Boltzmann distribution, causing the cloud to expand more rapidly. The temperature of atomic ensemble is correlated with the cloud's size in free-fall with the formula [55]:

$$\sigma^2(t_{\text{TOF}}) = \sigma_0^2 + \frac{k_B T}{m} t_{\text{TOF}}^2 \quad (4.1)$$

where σ is the cloud's size after t_{TOF} time, σ_0 is the initial cloud size, k_B is the Boltzmann constant and T is the temperature.

After the two-photon detuning scan, optimal power of Λ_{GMC} repumping light was found. The next optimization step was to find optimal time of Λ_{GMC} step duration. It was found to be 4 ms and it was set to that value in all the following measurements.

Later, the Λ_{GMC} cooler beam's intensity was optimized, and its optimal value was found to be 1.6 mW as it resulted in the smallest atomic cloud size as shown in Figure 4.2a. The measurement shows that as the Λ_{GMC} repumper to cooler intensity ratio increases, the cloud size increases, hence also the temperature. The temperature also increases when this ratio becomes too low, meaning that the Λ_{GMC} repumper intensity is not enough for efficient cooling.

It is a characteristic of Λ_{GMC} experiment that the lowest temperature is obtained while the two-photon detuning is equal to 0. It was shown for cesium atoms in [40]. Λ_{GMC} cooler frequency had a constant blue-shifted value while the frequency of the Λ_{GMC} repumper light was scanned. The same measurement was performed in our setup and the results are presented in Figure 4.2b. Indeed, the smallest cloud size is observed when the two-photon condition is met. The temperature behaviour for two-photon detuning scan is consistent with results in [40] and [36]. We observe that at blue-detuning from the two-photon condition, the temperature increases and reaches a peak value but decreases again when the detuning is further increased. Time of flight measurement and temperature calculation were performed at zero two-photon condition. Several iterations of the experiment were performed, in which size of the cloud was measured via absorption imaging. In each iteration, the time of flight

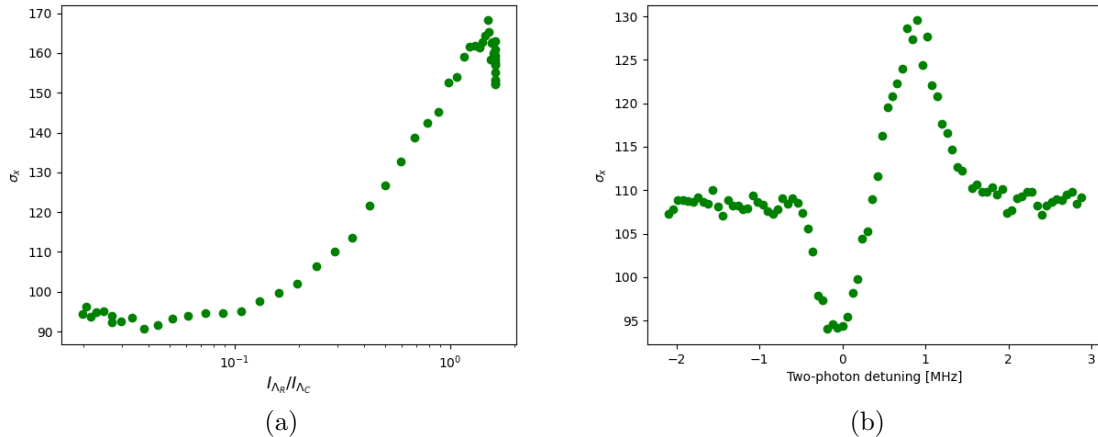


Figure 4.2: a) Atomic cloud's size dependence on the Λ_{GMC} repumper to Λ_{GMC} cooler intensity ratio. b) Atomic cloud's size as a function of two-photon detuning with Λ_{GMC} being scanned. $I_{\Lambda_{\text{C}}} = 1.6I_{\text{S}}$, $I_{\Lambda_{\text{R}}} = 0.06I_{\text{S}}$.

time-step had different duration. The time of flight dependency from equation 4.1 was fitted to the measurement results and the temperature of the atomic cloud after optimization of the Λ_{GMC} step was found to be 6.3 μK .

4.2. Observation of electromagnetically induced transparency

The STIRAP experimental setup was used to observe the electro-magnetically induced transparency. However, due to instabilities of the SL1 laser injection locked to the EOM sideband the alternative light path was used (Figure 2.7). Light from the EOM's output was sent directly to the double-pass path to obtain probe beam. During the measurements, the power of RF signal applied to EOM was equal to 19.5 dBm. As seen in the EOM's characteristic in Figure 2.2, for this power the carrier wave is strongly suppressed, while the $\pm 1\text{st}$ and $\pm 2\text{nd}$ sidebands have the same contribution, thus the $+1\text{st}$ sideband, with the desired frequency, makes up 25% of the EOM's output light intensity. The undesired sidebands were not filtered out from the beam, thus they were also present during the experiment. However, -1st and $\pm 2\text{nd}$ sidebands' frequencies are detuned far from atomic transitions in cesium, thus it was assumed that they do not interact with cesium atoms. The pump beam source was the SL2 laser operating at 113 mA and 39.8°C which was injection locked by seeding with 6.5 mW of unmodulated master laser light.

In the EIT experiment, a weaker probe and stronger pump light fields are used. Their frequencies are presented in Figure 4.3. The $+1\text{st}$ EOM's sideband was tuned to be resonant with the $F=3 \rightarrow F'=3$ transition after -220 MHz double pass in the AOM and it was used as a probe beam. The pump light beam was generated by SL2 laser injection locked with light coming directly from the master laser and frequency shifted by -270 MHz to be resonant with the $F=4 \rightarrow F'=3$ transition. The beams with orthogonal linear polarizations were coupled into one optical fiber.

The pump and probe light beams were sent to the main experimental chamber and focused on the atomic cloud. Their waist in the focus was reduced to 500 μm . Overlapped beams' position was later adjusted to pass through the atomic cloud after gray molasses cooling sequence. In order to do that, around 2 mW of pump light was used to observe its absorption

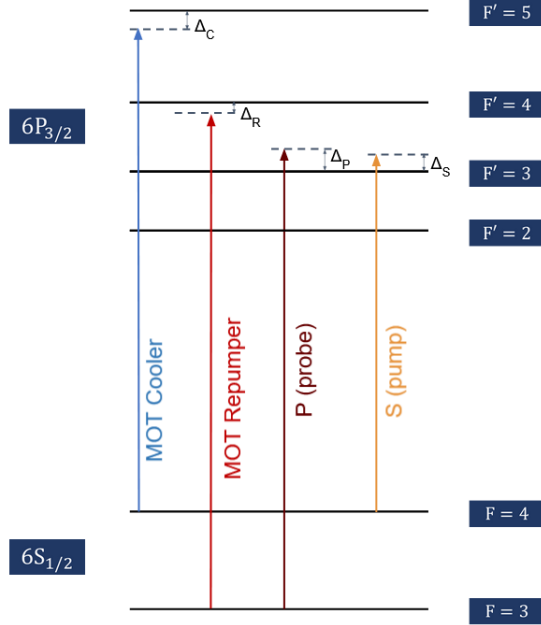


Figure 4.3: Light frequencies used in the experiment to observe electromagnetically induced transparency.

Table 4.2: Electromagnetically Induced Transparency experimental sequence. Intensities are expressed in terms of the saturation intensity, $I_S = 1.65 \text{ mW/cm}^2$.

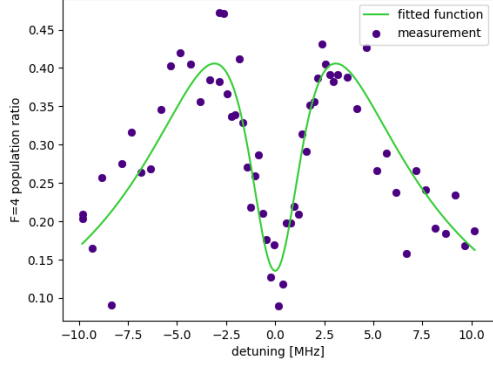
	B [G/cm]	I_C [I _S]	I_R [I _S]	Δ_C [MHz]	Δ_R [MHz]	Δ_S [MHz]	Δ_P [MHz]	T [μK]
MOT (5s)	15.1	14.7	4.2	-10.4	-10.4	-	-	230
CMOT (10ms)	31.1	14.7	4.2	-16.4	-16.4	-	-	-
GMC (25ms)	0	3.4	0.003	-221.5	0	-	-	10
EIT (0.5ms)	0	≤ 27	≤ 0.08	-	-	0	0	-

that 'burnt' a hole in the cloud, confirming that the beam passes through it.

The experimental sequence performed to observe electromagnetically induced transparency is shown in Table 4.2. First step was the magneto-optical trapping, which was followed by cloud compression in compressed magneto-optical trap step and cooling with grey molasses. Then, the EIT step was implemented, in which both pump and probe beams were turned on simultaneously for $500 \mu\text{s}$. Then, after 150 ms , the pump beam $500 \mu\text{s}$ was turned on again to excite atoms in $F=4$ ground state for purpose of fluorescence imaging. Probe and pump pulses duration, frequencies and intensities were controlled remotely by sending commands to the DG4000 Rigol signal generator.

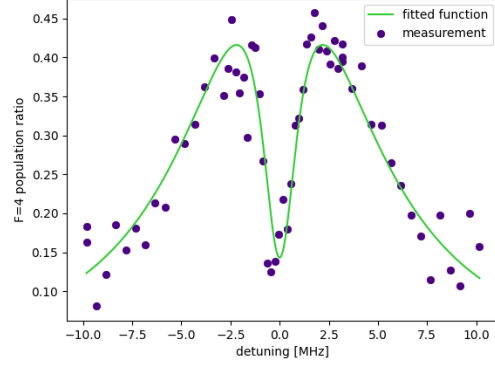
Several EIT spectra were measured for differing pump beam intensities ranging from $35.3 \mu\text{W}$ to $353.0 \mu\text{W}$ while probe beam's intensity had constant $0.95 \mu\text{W}$ value. The pump beam's detuning Δ_S was set to 0 and the probe beam's detuning Δ_P was scanned. The results are presented in Figure 4.4.

Number of atoms in $F=4$ ground state should fall to zero at zero two-photon detuning if no losses due to fluorescence occur. However, we can observe, that as the power of pump



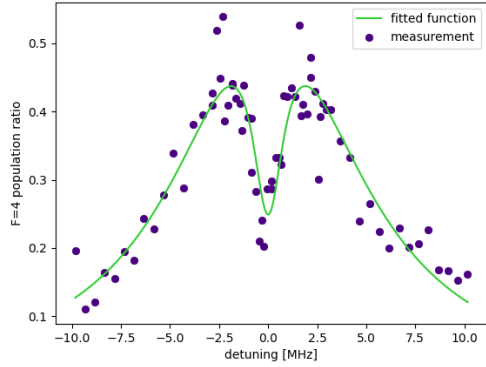
(a)

$$P_{\text{pump}}=353.0 \mu\text{W}, P_{\text{probe}}=0.95 \mu\text{W}, \\ \Omega_{\text{pump}}=2.18 \text{ MHz}, \Omega_{\text{probe}}=0.77 \text{ MHz}$$



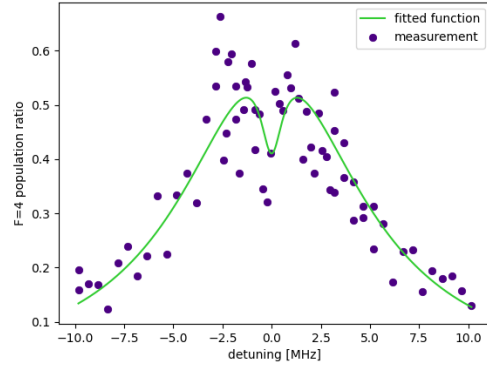
(b)

$$P_{\text{pump}}=247.1 \mu\text{W}, P_{\text{probe}}=0.95 \mu\text{W}, \\ \Omega_{\text{pump}}=1.41 \text{ MHz}, \Omega_{\text{probe}}=0.51 \text{ MHz}$$



(c)

$$P_{\text{pump}}=141.2 \mu\text{W}, P_{\text{probe}}=0.95 \mu\text{W}, \\ \Omega_{\text{pump}}=1.27 \text{ MHz}, \Omega_{\text{probe}}=0.59 \text{ MHz}$$



(d)

$$P_{\text{pump}}=35.3 \mu\text{W}, P_{\text{probe}}=0.95 \mu\text{W}, \\ \Omega_{\text{pump}}=0.96 \text{ MHz}, \Omega_{\text{probe}}=0.55 \text{ MHz}$$

Figure 4.4: Electromagnetically induced transparency spectra. The violet dots represent fluorescence signal from atoms excited from the F=4 ground state. The green line is a fitted theoretical curve taken from [44]. The population number is normalized with by a multiplicative constant found from the fitting parameters. The powers of pump and probe beams used in the experiment and respective Rabi frequencies Ω_{pump} and Ω_{probe} found by fitting the theoretical curves are enlisted in the captions under each graph.

light is decreased, more losses occur as the EIT dimple gets more shallow. Rabi frequencies corresponding to both pump and probe were deduced from the theoretical curve fitting [44], the same as used for simulations in Figure 1.8. As expected, Rabi oscillations due to pump beam increased with its power [42].

Chapter 5

Summary

We achieved phase coherence between two 852 nm laser light sources by means of injection locking. The sources were phase coherent both when they were optically injection locked with the same unmodulated light and when one of them was injection locked to the sideband of the seeding light modulated in an electro-optical modulator. However, injection locking with a sideband led to multimode operation of the laser. Perhaps these additional modes could be suppressed if the parameters like laser's operating current, temperature, seeding power and amplitude ratio of sidebands in the EOM output were scanned in wider range and checked for optimal performance.

With one of the laser injection locked to a sideband, we accomplished to implement Λ -enhanced gray molasses cooling and cool cesium atoms down to 6.3 μK . It was the first time to use this technique in our laboratory to cool cesium. We also managed to observe electromagnetically induced transparency with use of the setup for arbitrary optical pulses generation. The pulse generation process was fully automated and integrated into the software executing experimental sequences for the cold atoms experiments in the laboratory. In the future, we would like to use this setup to perform stimulated Raman adiabatic passage.

We also built and characterized operation of a 1064 nm laser module injection locked with master fiber laser light delivered with an optical circulator. Light from the module was later used to seed a fiber amplifier and beat-notes measurements were performed which confirmed that the output of the amplifier was phase coherent with the light from the module and also with the master fiber laser to which the module's laser diode was injection locked.

Bibliography

- [1] M. Fox, *Quantum Optics, An Introduction*. p. 16-19, 2006.
- [2] A. C. Bordonalli, *Optical injection phase-lock loops*. PhD thesis, University College London, p. 211, 1996.
- [3] “External cavity and distributed-feedback diode lasers.” <https://www.toptica.com/products/tunable-diode-lasers/ecdl-dfb-lasers/>. Accessed: 2021-10-14.
- [4] D. G. Matei, T. Legero, S. Häfner, C. Grebing, R. Weyrich, W. Zhang, L. Sonderhouse, J. M. Robinson, J. Ye, F. Riehle, and U. Sterr, “1.5 μm Lasers with Sub-10 mHz Linewidth,” *Phys. Rev. Lett.*, vol. 118, p. 263202, Jun 2017.
- [5] J. Yin, S. Zhu, W. Gao, and Y. Wang, “Relationship between temporal coherence and laser parameters in a two-longitudinal-mode hene laser,” *Applied Physics B*, vol. 63, pp. 8–11, 1996.
- [6] E. A. Donley, T. P. Heavner, F. Levi, M. O. Tataw, and S. R. Jefferts, “Double-pass acousto-optic modulator system,” *Review of Scientific Instruments*, vol. 76, no. 6, p. 063112, 2005.
- [7] C. Zhou, C. He, S.-T. Yan, Y.-H. Ji, L. Zhou, J. Wang, and M.-S. Zhan, “Laser frequency shift up to 5 GHz with a high-efficiency 12-pass 350-MHz acousto-optic modulator,” *Review of Scientific Instruments*, vol. 91, no. 3, p. 033201, 2020.
- [8] B. Lu and D. Wang, “Note: A four-pass acousto-optic modulator system for laser cooling of sodium atoms,” *Review of Scientific Instruments*, vol. 88, no. 7, p. 076105, 2017.
- [9] P. Yun, B. Tan, W. Deng, and S. Gu, “High coherent bi-chromatic laser with gigahertz splitting produced by the high diffraction orders of acousto-optic modulator used for coherent population trapping experiments,” *Review of Scientific Instruments*, vol. 82, no. 12, p. 123104, 2011.
- [10] E. de Carlos-López, J. M. López, S. López, M. G. Espinosa, and L. A. Lizama, “Note: Laser frequency shifting by using two novel triple-pass acousto-optic modulator configurations,” *Review of Scientific Instruments*, vol. 83, no. 11, p. 116102, 2012.
- [11] G.-C. Hsieh and J. Hung, “Phase-locked loop techniques. a survey,” *IEEE Transactions on Industrial Electronics*, vol. 43, no. 6, pp. 609–615, 1996.
- [12] W. Gunton, M. Semczuk, and K. W. Madison, “Method for independent and continuous tuning of N lasers phase-locked to the same frequency comb,” *Opt. Lett.*, vol. 40, pp. 4372–4375, Sep 2015.

- [13] S. T. Cundiff and J. Ye, “Colloquium: Femtosecond optical frequency combs,” *Rev. Mod. Phys.*, vol. 75, pp. 325–342, Mar 2003.
- [14] R. W. P. Drever, J. L. Hall, F. V. Kowalski, J. Hough, G. M. Ford, A. J. Munley, and H. Ward, “Laser phase and frequency stabilization using an optical resonator,” *Applied Physics B*, vol. 31, pp. 97–105, Jun 1983.
- [15] P. D. Gregory, P. K. Molony, M. P. Köppinger, A. Kumar, Z. Ji, B. Lu, A. L. Marchant, and S. L. Cornish, “A simple, versatile laser system for the creation of ultracold ground state molecules,” vol. 17, p. 055006, may 2015.
- [16] P. O. Leisher, C. Li, A. K. Jha, K. P. Pipe, J. D. Helmrich, P. Thiagarajan, M. C. Boisselle, S. K. Patra, S. Sezgin, and R. J. Deri, “Feedback-induced failure of high-power diode lasers,” *IEEE Journal of Quantum Electronics*, vol. 54, no. 6, pp. 1–13, 2018.
- [17] Z. Liu and R. Slavík, “Optical injection locking: From principle to applications,” *Journal of Lightwave Technology*, vol. 38, no. 1, pp. 43–59, 2020.
- [18] S. Wieczorek, W. Chow, L. Chrostowski, and C. Chang-Hasnain, “Improved semiconductor-laser dynamics from induced population pulsation,” *IEEE Journal of Quantum Electronics*, vol. 42, no. 6, pp. 552–562, 2006.
- [19] R. Kakarla, J. Schröder, and P. A. Andrekson, “Optical injection locking at sub nanowatt powers,” *Opt. Lett.*, vol. 43, pp. 5769–5772, Dec 2018.
- [20] V. Schkolnik, J. R. Williams, and N. Yu, “Generating 500 mw for laser cooling of strontium atoms by injection locking a high power laser diode,” *arXiv: Atomic Physics*, 2020.
- [21] H. B. Xue, Y. Y. Feng, X. J. Wang, S. Chen, and Z. Y. Zhou, “Note: Generation of raman laser beams based on a sideband injection-locking technique using a fiber electro-optical modulator,” *Review of Scientific Instruments*, vol. 84, no. 4, p. 046104, 2013.
- [22] X. Zhang, M. Huang, F. Zi, K. Huang, and X. hui Lu, “Generation of phase-locked beams by injection locking of extended-cavity diode lasers for atom interferometers,” *Applied Physics B*, vol. 126, pp. 1–5, 2020.
- [23] F. Wei, B. Lu, J. Wang, D. Xu, Z. Pan, D. Chen, H. Cai, and R. Qu, “Precision and broadband frequency swept laser source based on high-order modulation-sideband injection-locking,” *Opt. Express*, vol. 23, pp. 4970–4980, Feb 2015.
- [24] E. L. Raab, M. Prentiss, A. Cable, S. Chu, and D. E. Pritchard, “Trapping of neutral sodium atoms with radiation pressure,” *Physical Review Letters*, vol. 59, no. 23, pp. 2631–2634, 1987.
- [25] P. Arciszewski, “An experimental apparatus for laser cooling of potassium and caesium,” Master’s thesis, University of Warsaw, 2019.
- [26] D. A. Steck, “Cesium D line data,” 1998.
- [27] P. Palittapongarnpim, “Characterization of magneto-optical trap for experiments in light-atom interfacing,” p. 74, 2012.

- [28] K. Kowalski, V. C. Long, K. D. Xuan, M. Głódź, B. N. Huy, and J. Szonert, “Magneto-optical trap: Fundamentals and realization,” *computational methods in science and technology*, pp. 115–129, 2010.
- [29] M. Prevedelli, F. S. Cataliotti, E. A. Cornell, J. R. Ensher, C. Fort, L. Ricci, G. M. Tino, and M. Inguscio, “Trapping and cooling of potassium isotopes in a double-magneto-optical-trap apparatus,” *Phys. Rev. A*, vol. 59, pp. 886–888, Jan 1999.
- [30] D. C. McKay, D. Jervis, D. J. Fine, J. W. Simpson-Porco, G. J. A. Edge, and J. H. Thywissen, “Low-temperature high-density magneto-optical trapping of potassium using the open $4S \rightarrow 5P$ transition at 405 nm,” *Physical Review A*, vol. 84, Dec 2011.
- [31] J. C. J. Koelemeij, R. J. W. Stas, W. Hogervorst, and W. Vassen, “Magneto-optical trap for metastable helium at 389 nm,” *Physical Review A*, vol. 67, May 2003.
- [32] R. Hobson, W. Bowden, A. Vianello, I. R. Hill, and P. Gill, “Midinfrared magneto-optical trap of metastable strontium for an optical lattice clock,” *Physical Review A*, vol. 101, Jan 2020.
- [33] W. D. Phillips, “Nobel lecture: Laser cooling and trapping of neutral atoms,” *Rev. Mod. Phys.*, vol. 70, pp. 721–741, Jul 1998.
- [34] P. D. Lett, W. D. Phillips, S. L. Rolston, C. E. Tanner, R. N. Watts, and C. I. Westbrook, “Optical molasses,” *J. Opt. Soc. Am. B*, vol. 6, pp. 2084–2107, Nov 1989.
- [35] B. Shammout, “A laser system for gray-molasses cooling on the D1 transition of an atomic gas of 39K,” Master’s thesis, Leibniz Hannover University, 2019.
- [36] S. Rosi, A. Burchianti, S. Conclave, D. S. Naik, G. Roati, C. Fort, and F. Minardi, “ Λ -enhanced grey molasses on the D2 transition of Rubidium-87 atoms,” *Scientific Reports*, vol. 8, Jan 2018.
- [37] D. Rio Fernandes, F. Sievers, N. Kretzschmar, S. Wu, C. Salomon, and F. Chevy, “Sub-Doppler laser cooling of fermionic 40K atoms in three-dimensional gray optical molasses,” *EPL (Europhysics Letters)*, vol. 100, p. 63001, Dec 2012.
- [38] D. Nath, R. K. Easwaran, G. Rajalakshmi, and C. S. Unnikrishnan, “Quantum-interference-enhanced deep sub-doppler cooling of 39K atoms in gray molasses,” *Physical Review A*, vol. 88, Nov 2013.
- [39] H.-Z. Chen, X.-C. Yao, Y.-P. Wu, X.-P. Liu, X.-Q. Wang, Y.-X. Wang, Y.-A. Chen, and J.-W. Pan, “Production of large K41 bose-einstein condensates using D1 gray molasses,” *Physical Review A*, vol. 94, Sep 2016.
- [40] Y.-F. Hsiao, Y.-J. Lin, and Y.-C. Chen, “ Λ -enhanced gray-molasses cooling of cesium atoms on the D_2 line,” *Phys. Rev. A*, vol. 98, p. 033419, Sep 2018.
- [41] A. T. Grier, I. Ferrier-Barbut, B. S. Rem, M. Delehaye, L. Khaykovich, F. Chevy, and C. Salomon, “ Λ -enhanced sub-Doppler cooling of lithium atoms in D1 gray molasses,” *Physical Review A*, vol. 87, Jun 2013.
- [42] M. Fleischhauer, A. Imamoglu, and J. P. Marangos, “Electromagnetically induced transparency: Optics in coherent media,” *Rev. Mod. Phys.*, vol. 77, pp. 633–673, Jul 2005.

- [43] N. V. Vitanov, A. A. Rangelov, B. W. Shore, and K. Bergmann, “Stimulated raman adiabatic passage in physics, chemistry, and beyond,” *Rev. Mod. Phys.*, vol. 89, p. 015006, Mar 2017.
- [44] S. Sen, T. K. Dey, M. R. Nath, and G. Gangopadhyay, “Comparison of electromagnetically induced transparency in lambda, cascade and vee three-level systems,” *Journal of Modern Optics*, vol. 62, p. 166–174, Sep 2014.
- [45] M. Bass, *Handbook of Optics, Devices, Measurements, & Properties, Second Edition, Volume II*. se. 13.19, 1995.
- [46] “Application Note: Practical Uses and Applications of Electro-Optic Modulators.” <https://www.newport.com/n/practical-uses-and-applications-of-electro-optic-modulators>. Accessed: 2021-10-11.
- [47] P. Debye and F. W. Sears, “On the scattering of light by supersonic waves,” *Proceedings of the National Academy of Sciences*, vol. 18, no. 6, pp. 409–414, 1932.
- [48] P. Albrodt, M. T. Jamal, A. K. Hansen, O. B. Jensen, G. Blume, K. Paschke, P. A. Crump, P. M. Georges, and G. Lucas-Leclin, “Coherent combining of high brightness tapered amplifiers for efficient non-linear conversion.,” *Optics express*, vol. 27 2, pp. 928–937, 2019.
- [49] T. Shimasaki, E. R. Edwards, and D. DeMille, “Injection-locking of a fiber-pigtailed high-power laser to an external cavity diode laser via a fiber optic circulator,” *Review of Scientific Instruments*, vol. 90, p. 056102, May 2019.
- [50] “Photonics Technical Note # 25, Fiber Optics fiber optics: How fused fiber optic couplers work.” https://www.newport.com/medias/sys_master/images/images/h86/hb2/8797287088158/Tech-Note-26-How-Fused-Fiber-Optic-Couplers-Work.pdf. Accessed: 2021-10-02.
- [51] N. Miura, *Comprehensive Semiconductor Science and Technology*. 2011.
- [52] “DK Photonics Blog, What is Optical Circulator? What is the application of Optical Circulator?.” <http://www.dkphotonics.com/blog/optical-circulator-application-optical-circulator/>. Accessed: 2021-10-02.
- [53] V. I. Balykin, V. G. Minogin, and V. S. Letokhov, “Electromagnetic trapping of cold atoms,” vol. 63, pp. 1429–1510, aug 2000.
- [54] P. Albrodt, M. T. Jamal, A. K. Hansen, O. B. Jensen, G. Blume, K. Paschke, P. Crump, P. Georges, and G. Lucas-Leclin, “Coherent combining of high brightness tapered amplifiers for efficient non-linear conversion,” *Opt. Express*, vol. 27, pp. 928–937, Jan 2019.
- [55] T. M. Brzozowski, M. Maczynska, M. Zawada, J. Zachorowski, and W. Gawlik, “Time-of-flight measurement of the temperature of cold atoms for short trap-probe beam distances,” vol. 4, pp. 62–66, jan 2002.